NOVEL STRATEGIES FOR SECOND-KIND INTEGRAL EQUATIONS TO ANALYZE PERFECT ELECTRIC CONDUCTORS

A THESIS SUBMITTED TO
THE GRADUATE SCHOOL OF NATURAL AND APPLIED SCIENCES
OF
MIDDLE EAST TECHNICAL UNIVERSITY

BY

SADRİ GÜLER

IN PARTIAL FULFILLMENT OF THE REQUIREMENTS
FOR
THE DEGREE OF MASTER OF SCIENCE
IN
ELECTRICAL AND ELECTRONICS ENGINEERING

SEPTEMBER 2019

Approval of the thesis:

NOVEL STRATEGIES FOR SECOND-KIND INTEGRAL EQUATIONS TO ANALYZE PERFECT ELECTRIC CONDUCTORS

submitted by **SADRİ GÜLER** in partial fulfillment of the requirements for the degree of **Master of Science in Electrical and Electronics Engineering Department, Middle East Technical University** by,

Prof. Dr. Halil Kalıpçılar
Dean, Graduate School of **Natural and Applied Sciences** _____

Prof. Dr. İlkay Ulusoy
Head of Department, **Electrical and Electronics Engineering** _____

Assoc. Prof. Dr. Özgür Ergül
Supervisor, **Electrical and Electronics Engineering, METU** _____

Examining Committee Members:

Prof. Dr. Sencer Koç
Electrical and Electronics Engineering, METU _____

Assoc. Prof. Dr. Özgür Ergül
Electrical and Electronics Engineering, METU _____

Assoc. Prof. Dr. Lale Alatan
Electrical and Electronics Engineering, METU _____

Prof. Dr. Vakur Behçet Ertürk
Electrical and Electronics Engineering, Bilkent University _____

Assoc. Prof. Dr. Fatih Dikmen
Electronics Engineering, Gebze Technical University _____

Date:

I hereby declare that all information in this document has been obtained and presented in accordance with academic rules and ethical conduct. I also declare that, as required by these rules and conduct, I have fully cited and referenced all material and results that are not original to this work.

Name, Surname: Sadri Güler

Signature :

ABSTRACT

NOVEL STRATEGIES FOR SECOND-KIND INTEGRAL EQUATIONS TO ANALYZE PERFECT ELECTRIC CONDUCTORS

Güler, Sadri
M.S., Department of Electrical and Electronics Engineering
Supervisor: Assoc. Prof. Dr. Özgür Ergül

September 2019, 62 pages

In this thesis, the magnetic-field integral equation (MFIE) for three-dimensional perfectly conducting objects is studied with a particular focus on the solutions of the formulation with the method of moments employing low-order discretization elements. Possible discretization functions and their applications in the testing of MFIE while considering different numbers of testing points are analyzed for accurate and efficient solutions. Successful results are obtained by using rotational Buffa-Christiansen testing functions when the electric current density is expanded with Rao-Wilton-Glisson functions. The same mixed discretization scheme is also employed in the context of the combined-field integral equation (CFIE). In order to successfully handle internal resonances in the mixed-discretized CFIE, projection of testing spaces of EFIE and MFIE via Gram matrices is required. Inversion of Gram matrices is discussed in terms of computational requirements in the context of large-scale problems analyzed with the multilevel fast multipole algorithm (MLFMA). Finally, a novel MFIE implementation with double-layer modeling is presented to mitigate internal resonances without resorting to CFIE. Accuracy of the proposed formulation is improved via inner-layer

selection, post-processing, and accurate discretization techniques. All discussions are presented and supported via numerical results involving canonical objects.

Keywords: Surface Integral Equations, Magnetic-Field Integral Equation, Discretization of Integral Equations, Matrix Decomposition Methods, Gram Matrix, Internal Resonance Problem

ÖZ

MÜKEMMEL İLETKENLERİN ANALİZLERİNDE İKİNCİ TÜRDEN İNTEGRAL DENKLEMLERİ İÇİN YENİLİKÇİ STRATEJİLER

Güler, Sadri
Yüksek Lisans, Elektrik ve Elektronik Mühendisliği Bölümü
Tez Yöneticisi: Doç. Dr. Özgür Ergül

Eylül 2019, 62 sayfa

Bu çalışmada, üç boyutlu mükemmel iletken cisimler için manyetik alan integral denklemi (MAİD), bu formülasyonun düşük dereceli ayrıklaştırma elemanlarının kullanıldığı momentler metoduyla çözümlerine yoğunlaşılarak ele alınmıştır. Muhtemel ayrıklaştırma fonksiyonları ve bu fonksiyonların MAİD'nin test edilmesinde kullanılması, çeşitli sayılardaki test noktalarının da göz önüne alınmasıyla doğruluk ve verimlilik açısından analiz edilmiştir. Elektrik akımının Rao-Wilton-Glisson fonksiyonlarıyla açıldığı durumlarda, döngü Buffa-Christiansen test fonksiyonlarının kullanılmasıyla başarılı sonuçlar elde edilmiştir. Geliştirilen karışık ayrıklaştırma yöntemi, birleşik alan integral denklemi (BAİD) için de kullanılmıştır. Karışık ayrıklaştırma yöntemini BAİD üzerinde kullanırken iç rezonans problemlerinden başarıyla kaçınmak için test uzaylarının Gram matrisleri vasıtasıyla yansıtılması gerekmektedir. Büyük ölçekli problemlerin çok seviyeli hızlı çokkutup yöntemiyle analizleri kapsamında, Gram matrislerinin terslerinin alınması sayısal hesaplama gereksinimleri bakımından incelenmiştir. Son olarak, yeni bir çift katmanlı MAİD yaklaşımı mükemmel iletken cisimlerin analizlerinde iç rezonans problemlerini BAİD'ye ihtiyaç duymadan orta-

dan kaldırmak için önerilmiştir. Önerilen bu formülasyonun doğruluğu, iç katman seçimi, art işleme, ve uygun ayrıklaştırma teknikleri ile iyileştirilmiştir. Tüm tartışmalar kanonik cisimler üzerinde sayısal sonuçlarla desteklenmiştir.

Anahtar Kelimeler: Yüzey İntegral Denklemleri, Manyetik Alan İntegral Denklemi, İntegral Denklemlerinin Ayrıklaştırılması, Matris Ayrıştırma Yöntemleri, Gram Matrisi, İç Rezonans Problemi

In memory of my grand-dad Ali Osman Güler,

ACKNOWLEDGMENTS

Throughout the writing of this thesis I have received a great deal of support and assistance. I would like to thank my supervisor, Dr. Özgür Ergül, who has given me the chance to work with him, always shared his expertise with me, and always been more than a supervisor.

I would also like to thank Prof. Dr. Sencer Koç, Assoc. Prof. Dr. Lale Alatan, Prof. Dr. Vakur Ertürk, and Assoc. Prof. Dr. Fatih Dikmen for accepting to be a part of my thesis committee and their valuable comments and suggestions.

I owe and respectfully offer my thanks to Dr. Hakan Bağcı for showing a different perspective of how-to-do a research and his endless supports.

I would like to thank TÜBİTAK for the 2210-A scholarship program for supporting the writing process of this thesis.

I have been part of the group "Computational Electromagnetics at Middle East Technical University" (CEMMETU) for nearly six years. This thesis would not have been possible without the inspiration and support of the individuals of CEMMETU. In this group, I have gained great friends and colleagues, and I want to thank all members of CEMMETU for their great collaboration, patience, and expertise. Some special word of thanks goes to Barışcan, Hande, Meriç, Ali, Feza, Türker, Şirin, Özgür, Gökhan, and Göktuğ. I am deeply thankful to Zeina El-Ahdab Jr. for making the last year easier in all aspects for me.

It is a pleasure to thank Sezer Caymaz for not just being a great friend but also for being part of the family! The last words go to my mom Sezer, dad Basri, and brother Serdar for always letting me know that they are always with me to help and support me, and for everything, which words are not enough to explain!

TABLE OF CONTENTS

LIST OF FIGURES

FIGURES

LIST OF ABBREVIATIONS

BC	Buffa-Christiansen
CFIE	Combined-field integral equation
EFIE	Electric-field integral equation
MFIE	Magnetic-field integral equation
MFIE-DL	Magnetic-field integral equation with double layer
MLFMA	Multilevel fast multipole algorithm
PEC	Perfect electric conductor
RWG	Rao-Wilton-Glisson
rot-BC	Rotated Buffa-Christiansen
rot-RWG	Rotated Rao-Wilton-Glisson
SIE	Surface integral equation

CHAPTER 1

INTRODUCTION

Full-wave methods in computational electromagnetics can generally be categorized into two groups, i.e., methods based on differential equations and those based on integral equations. The method of moments is particularly used to solve electromagnetic problems formulated with integral equations. For the analysis of perfect electric conductors (PECs), the electric-field integral equation (EFIE) and the magnetic-field integral equation (MFIE) are two commonly used surface integral equations. For closed conductors, a linear combination of these integral equations, namely, the combined-field integral equation (CFIE), is preferred to avoid internal resonances.

The main focus of this thesis is MFIE, particularly considering its accuracy and iterative solutions, for three-dimensional PECs. We start with a topic that has recently attracted great interest, i.e., correct testing of MFIE. We present a mixed discretization of MFIE, which involves the use of different sets of basis and testing functions to reach accurate solutions. The mixed discretization is also extended to CFIE, while projection of subspaces is needed to properly combine MFIE and EFIE. The thesis also includes a novel double-layer modeling, which enables resonance-free formulations only with MFIE.

Before starting the main content of the thesis, we introduce some fundamental information on Maxwell's equations, surface integral equations (SIEs), and the method of moments, as follows.

1.1 Surface Integral Equations

In electromagnetics, at any point in the space represented by $\boldsymbol{r}$ and at any time t, Faraday's law is written as

$$\nabla \times \boldsymbol{E}(\boldsymbol{r}, t) = -\frac{\partial \boldsymbol{B}(\boldsymbol{r}, t)}{\partial t}, \tag{1.1}$$

where $\boldsymbol{E}(\boldsymbol{r}, t)$ represents the electric field intensity and $\boldsymbol{B}(\boldsymbol{r}, t)$ represents the magnetic flux density. Similarly, Ampere's law is written as

$$\nabla \times \boldsymbol{H}(\boldsymbol{r}, t) = \frac{\partial \boldsymbol{D}(\boldsymbol{r}, t)}{\partial t} + \boldsymbol{J}(\boldsymbol{r}, t), \tag{1.2}$$

where $\boldsymbol{H}(\boldsymbol{r}, t)$ represents the magnetic field intensity, $\boldsymbol{D}(\boldsymbol{r}, t)$ represents the electric flux density, and $\boldsymbol{J}(\boldsymbol{r}, t)$ represents the electric current density. Gauss's law defines the relationship between the electric flux density ($\boldsymbol{D}(\boldsymbol{r}, t)$) and the electric charge density ($\rho_e(\boldsymbol{r}, t)$) as

$$\nabla \cdot \boldsymbol{D}(\boldsymbol{r}, t) = \rho_e(\boldsymbol{r}, t). \tag{1.3}$$

Similarly, in the absence of magnetic sources, the divergence of the magnetic flux density can be written as

$$\nabla \cdot \boldsymbol{B}(\boldsymbol{r}, t) = 0. \tag{1.4}$$

Equations (1.1), (1.2), (1.3), and (1.4) given above form Maxwell's equations in time domain. The continuity equation can be obtained by taking the divergence of (1.2), and then using with (1.3). Thus, it defines the relationship between the electric current and charge densities as

$$\nabla \cdot \boldsymbol{J}(\boldsymbol{r}, t) = -\frac{\partial \rho_e(\boldsymbol{r}, t)}{\partial t}. \tag{1.5}$$

For a linear and isotropic medium, constitutive relations, which represent the dependencies between the flux densities and field intensities for electric and magnetic fields can be written as

$$\boldsymbol{D}(\boldsymbol{r}, t) = \epsilon \boldsymbol{E}(\boldsymbol{r}, t) \tag{1.6a}$$

$$\boldsymbol{B}(\boldsymbol{r}, t) = \mu \boldsymbol{H}(\boldsymbol{r}, t). \tag{1.6b}$$

By substituting the constitutive relations, Maxwell's equations can be expressed only in terms of the electric and magnetic field intensity, which can be written as

$$\nabla \times \boldsymbol{E}(\boldsymbol{r},t) = -\mu \frac{\partial \boldsymbol{H}(\boldsymbol{r},t)}{\partial t} \tag{1.7a}$$

$$\nabla \times \boldsymbol{H}(\boldsymbol{r},t) = \epsilon \frac{\partial \boldsymbol{E}(\boldsymbol{r},t)}{\partial t} + \boldsymbol{J}(\boldsymbol{r},t) \tag{1.7b}$$

$$\nabla \cdot \boldsymbol{E}(\boldsymbol{r},t) = \frac{1}{\epsilon}\rho_e(\boldsymbol{r},t) \tag{1.7c}$$

$$\nabla \cdot \boldsymbol{H}(\boldsymbol{r},t) = 0. \tag{1.7d}$$

Time-harmonic electromagnetic waves and their derivatives can be expressed in simplified forms, while transformations for any wave function $f(\boldsymbol{r},t)$ can be defined as

$$f(\boldsymbol{r},t) = Re\{f(\boldsymbol{r})e^{-i\omega t}\} \tag{1.8a}$$

$$\frac{\partial f(\boldsymbol{r},t)}{\partial t} = -i\omega Re\{f(\boldsymbol{r})e^{-i\omega t}\}, \tag{1.8b}$$

where $f(\boldsymbol{r})$ is the phasor representation of $f(\boldsymbol{r},t)$. By using (1.8a) and (1.8b), Maxwell's equations can be written in phasor domain as

$$\nabla \times \boldsymbol{E}(\boldsymbol{r}) = i\omega\mu \boldsymbol{H}(\boldsymbol{r}) \tag{1.9a}$$

$$\nabla \times \boldsymbol{H}(\boldsymbol{r}) = -i\omega\epsilon \boldsymbol{E}(\boldsymbol{r}) + \boldsymbol{J}(\boldsymbol{r}) \tag{1.9b}$$

$$\nabla \cdot \boldsymbol{E}(\boldsymbol{r}) = \frac{1}{\epsilon}\rho_e(\boldsymbol{r}) \tag{1.9c}$$

$$\nabla \cdot \boldsymbol{H}(\boldsymbol{r}) = 0 \tag{1.9d}$$

$$\nabla \cdot \boldsymbol{J}(\boldsymbol{r}) = i\omega\rho_e(\boldsymbol{r}) \tag{1.9e}$$

using phasor representation of all quantities. Due to the solenoidal nature of the magnetic flux density in (1.4), it can be written as

$$\boldsymbol{B}(\boldsymbol{r}) = \nabla \times \boldsymbol{A}(\boldsymbol{r}), \tag{1.10}$$

where $\boldsymbol{A}(\boldsymbol{r})$ is the magnetic vector potential. Substituting the constitutive relation (1.6b) into (1.10), the magnetic field intensity is represented in terms of the magnetic vector potential as

$$\boldsymbol{H}(\boldsymbol{r}) = \frac{1}{\mu}\nabla \times \boldsymbol{A}(\boldsymbol{r}). \tag{1.11}$$

Substituting (1.11) into (1.9a), the electric field intensity can be represented in terms of the electric scalar potential and the magnetic vector potential as

$$\boldsymbol{E}(\boldsymbol{r}) = -\nabla V(\boldsymbol{r}) + i\omega \boldsymbol{A}(\boldsymbol{r}). \tag{1.12}$$

Then, substituting (1.12) and (1.11) into (1.9b), we derive

$$\nabla \times \Big(\frac{1}{\mu}\nabla \times \boldsymbol{A}(\boldsymbol{r})\Big) = -i\omega\epsilon(-\nabla V(\boldsymbol{r}) + i\omega \boldsymbol{A}(\boldsymbol{r})) + \boldsymbol{J}(\boldsymbol{r}) \tag{1.13a}$$

$$\nabla \times \nabla \times \boldsymbol{A}(\boldsymbol{r}) = i\omega\epsilon\mu\nabla V(\boldsymbol{r}) + \omega^2\epsilon\mu\boldsymbol{A}(\boldsymbol{r}) + \mu\boldsymbol{J}(\boldsymbol{r}) \tag{1.13b}$$

$$\nabla(\nabla \cdot \boldsymbol{A}(\boldsymbol{r})) - \nabla^2\boldsymbol{A}(\boldsymbol{r}) = i\omega\epsilon\mu\nabla V(\boldsymbol{r}) + \omega^2\epsilon\mu\boldsymbol{A}(\boldsymbol{r}) + \mu\boldsymbol{J}(\boldsymbol{r}) \tag{1.13c}$$

$$\nabla(\nabla \cdot \boldsymbol{A}(\boldsymbol{r})) - i\omega\epsilon\mu\nabla V(\boldsymbol{r}) = \nabla^2\boldsymbol{A}(\boldsymbol{r}) + \omega^2\epsilon\mu\boldsymbol{A}(\boldsymbol{r}) + \mu\boldsymbol{J}(\boldsymbol{r}). \tag{1.13d}$$

In order to express (1.13d) only in terms of $\boldsymbol{A}(\boldsymbol{r})$, Lorentz's gauge can be used to write

$$\nabla \cdot \boldsymbol{A}(\boldsymbol{r}) = i\omega\epsilon\mu V(\boldsymbol{r}). \tag{1.14}$$

Then, the Helmholtz equation for the magnetic vector potential can be written as

$$\nabla^2\boldsymbol{A}(\boldsymbol{r}) + k^2\boldsymbol{A}(\boldsymbol{r}) = -\mu\boldsymbol{J}(\boldsymbol{r}), \tag{1.15}$$

where $k = \omega\sqrt{\epsilon\mu} = 2\pi/\lambda$ is the wavenumber and λ is the wavelength. The point-source solution of the scalar Helmholtz equation for an isotropic, linear, and homogeneous media is

$$g(\boldsymbol{r}, \boldsymbol{r}') = \frac{e^{ik|\boldsymbol{r}-\boldsymbol{r}'|}}{4\pi|\boldsymbol{r}-\boldsymbol{r}'|}, \tag{1.16}$$

which is known as the three-dimensional Green's function. Then, the magnetic vector potential caused by an electric current density distribution can be written as

$$\boldsymbol{A}(\boldsymbol{r}) = \mu \int g(\boldsymbol{r}, \boldsymbol{r}')\boldsymbol{J}(\boldsymbol{r}')d\boldsymbol{r}'. \tag{1.17}$$

Similarly, the electric scalar potential caused by an electric charge density distribution can be written as

$$V(\boldsymbol{r}) = \frac{1}{\epsilon}\int g(\boldsymbol{r}, \boldsymbol{r}')\rho_e(\boldsymbol{r}')d\boldsymbol{r}'. \tag{1.18}$$

Substituting (1.17) and (1.18) into (1.12), the electric field intensity can also be written as

$$\boldsymbol{E}(\boldsymbol{r}) = -\nabla\Big(\frac{1}{\epsilon}\int g(\boldsymbol{r}, \boldsymbol{r}')\rho_e(\boldsymbol{r}')d\boldsymbol{r}'\Big) + i\omega\mu\int g(\boldsymbol{r}, \boldsymbol{r}')\boldsymbol{J}(\boldsymbol{r}')d\boldsymbol{r}'. \tag{1.19}$$

Applying the continuity equation and rearranging the terms in (1.19), the electric field intensity can be written as

$$\boldsymbol{E}(\boldsymbol{r}) = \frac{i}{\omega\epsilon}\int \nabla g(\boldsymbol{r}, \boldsymbol{r}')\nabla' \cdot \boldsymbol{J}(\boldsymbol{r}')d\boldsymbol{r}' + i\omega\mu\int g(\boldsymbol{r}, \boldsymbol{r}')\boldsymbol{J}(\boldsymbol{r}')d\boldsymbol{r}' \tag{1.20}$$

or

$$\boldsymbol{E}(\boldsymbol{r}) = ik\eta \int \Big[\boldsymbol{J}(\boldsymbol{r}') + \frac{1}{k^2}\,\nabla' \cdot \boldsymbol{J}(\boldsymbol{r}')\nabla\Big] g(\boldsymbol{r}, \boldsymbol{r}')d\boldsymbol{r}', \tag{1.21}$$

where $\eta = \sqrt{\mu/\epsilon}$ represents the intrinsic impedance. Similarly, the magnetic field intensity can be written in terms of the current density and the Green's function as

$$\boldsymbol{H}(\boldsymbol{r}) = \int \nabla g(\boldsymbol{r}, \boldsymbol{r}') \times \boldsymbol{J}(\boldsymbol{r}')d\boldsymbol{r}'. \tag{1.22}$$

Defining the integro-differential operators as

$$\boldsymbol{\mathcal{T}}\{\boldsymbol{X}\}(\boldsymbol{r}) = ik \int \Big[\boldsymbol{X}(\boldsymbol{r}') + \frac{1}{k^2}\,\nabla' \cdot \boldsymbol{X}(\boldsymbol{r}')\nabla\Big] g(\boldsymbol{r}, \boldsymbol{r}')d\boldsymbol{r}' \tag{1.23a}$$

$$\boldsymbol{\mathcal{K}}\{\boldsymbol{X}\}(\boldsymbol{r}) = \int \nabla g(\boldsymbol{r}, \boldsymbol{r}') \times \boldsymbol{X}(\boldsymbol{r}')d\boldsymbol{r}', \tag{1.23b}$$

the electric and magnetic field intensities can be written shortly as

$$\boldsymbol{E}(\boldsymbol{r}) = \eta\boldsymbol{\mathcal{T}}\{\boldsymbol{J}\}(\boldsymbol{r}) \tag{1.24a}$$

$$\boldsymbol{H}(\boldsymbol{r}) = \boldsymbol{\mathcal{K}}\{\boldsymbol{J}\}(\boldsymbol{r}). \tag{1.24b}$$

The equivalence principle states that an electromagnetic problem can be converted into equivalent problems by defining equivalent surface currents ($\boldsymbol{J}(\boldsymbol{r})$) on the surfaces. Although the hypothetical surfaces can be defined anywhere, they are practically chosen to coincide with actual surfaces to apply physical boundary conditions. Consider a PEC placed in a homogeneous medium with permittivity ϵ and permeability μ. Boundary conditions state that tangential electric fields are continuous, and for a PEC object, this can be written as

$$0 = \hat{\boldsymbol{n}} \times \hat{\boldsymbol{n}} \times \boldsymbol{E}^{inc}(\boldsymbol{r}) + \hat{\boldsymbol{n}} \times \hat{\boldsymbol{n}} \times \boldsymbol{E}^{sec}(\boldsymbol{r}) \tag{1.25}$$

considering that fields do not penetrate into the object. In the above, $\boldsymbol{E}^{inc}$ is incident electric field intensity, $\boldsymbol{E}^{sec}(\boldsymbol{r})$ is the secondary electric field intensity due to the equivalence currents, and $\hat{\boldsymbol{n}}$ is unit normal vector on the surface. Modifying (1.25) and writing $\boldsymbol{E}^{sec}(\boldsymbol{r})$ in terms of equivalent currents, tangential electric-field integral equation (T-EFIE) can be written as

$$-\eta\hat{\boldsymbol{n}} \times \hat{\boldsymbol{n}} \times \boldsymbol{\mathcal{T}}\{\boldsymbol{J}\}(\boldsymbol{r}) = \hat{\boldsymbol{n}} \times \hat{\boldsymbol{n}} \times \boldsymbol{E}^{inc}(\boldsymbol{r}). \tag{1.26}$$

Similarly, by sampling the rotated version of the tangential magnetic field intensity, and using the related boundary condition, the normal magnetic-field integral equation (N-MFIE) for a PEC object can be written as

$$-\boldsymbol{J}(\boldsymbol{r}) + \hat{\boldsymbol{n}} \times \boldsymbol{\mathcal{K}}\{\boldsymbol{J}\}(\boldsymbol{r}) = -\hat{\boldsymbol{n}} \times \boldsymbol{H}^{inc}(\boldsymbol{r}). \tag{1.27}$$

1.2 Method of Moments

Surface integral equations can be considered in a general form as

$$\boldsymbol{\mathcal{L}}\{\boldsymbol{J}\}(\boldsymbol{r}) = \boldsymbol{g}(\boldsymbol{r}), \tag{1.28}$$

where $\boldsymbol{\mathcal{L}}$ is a linear operator applied on the current density $\boldsymbol{J}(\boldsymbol{r})$ to obtain known vector function $\boldsymbol{g}(\boldsymbol{r})$. To obtain matrix equations, $\boldsymbol{J}(\boldsymbol{r})$ is expanded as a linear combination of a set of spatial basis functions $\boldsymbol{b}_n(\boldsymbol{r})$ as

$$\boldsymbol{J}(\boldsymbol{r}) \approx \sum_{n=1}^{N} a_n \boldsymbol{b}_n(\boldsymbol{r}), \tag{1.29}$$

where N is the number of discretization functions and a_n represents the unknown coefficient of each function to expand the current density. Substituting (1.29) into (1.28), we obtain

$$\sum_{n=1}^{N} a_n \boldsymbol{\mathcal{L}}\{\boldsymbol{b}_n(\boldsymbol{r})\} = \boldsymbol{g}(\boldsymbol{r}). \tag{1.30}$$

Equation (1.30) involves N unknowns within a single equation. By taking the inner product of (1.30) with linearly independent testing functions $\boldsymbol{t}_m(\boldsymbol{r})$, we obtain the required number of equations to solve coefficients a_n as

$$\int d\boldsymbol{r} \boldsymbol{t}_m(\boldsymbol{r}) \cdot \sum_{n=1}^{N} a_n \boldsymbol{\mathcal{L}}\{\boldsymbol{b}_n(\boldsymbol{r})\} = \int d\boldsymbol{r} \boldsymbol{t}_m(\boldsymbol{r}) \cdot \boldsymbol{g}(\boldsymbol{r}) d\boldsymbol{r} \tag{1.31}$$

for $m = 1, 2, ..., N$. The formulation given above can be further expressed as a matrix equation, i.e.,

$$\bar{\boldsymbol{Z}} \cdot \boldsymbol{x} = \boldsymbol{w}, \tag{1.32}$$

where

$$\bar{\boldsymbol{Z}}[m, n] = \int d\boldsymbol{r} \boldsymbol{t}_m(\boldsymbol{r}) \cdot \boldsymbol{\mathcal{L}}\{\boldsymbol{b}_n(\boldsymbol{r})\} \tag{1.33a}$$

$$\boldsymbol{x}[n] = a_n \tag{1.33b}$$

$$\boldsymbol{w}[m] = \int d\boldsymbol{r} \boldsymbol{t}_m(\boldsymbol{r}) \cdot \boldsymbol{g}(\boldsymbol{r}) d\boldsymbol{r}. \tag{1.33c}$$

1.3 On the Accuracy of Numerical Solutions of Surface Integral Equations

SIEs are often classified as first-kind and second-kind Fredholm integral equations. For the analysis of PEC objects, EFIE is known as a first-kind integral equation, while

MFIE is known as a second-kind integral equation. Using a Galerkin discretization scheme by employing low-order discretization elements, first-kind integral equations generally provide accurate results with large numbers of iterations, while second-kind integral equations provide very good convergence rates but less accurate results. In last 30 years, researchers in this area have studied EFIE to accelerate its iterative solutions and MFIE to improve its accuracy.

Both EFIE and MFIE suffer from internal resonances which lead to significantly inaccurate solutions and/or large numbers of iterations at resonance frequencies. It is known that resonance currents of EFIE do not radiate to far zone, so it still satisfies accurate far-field scattering results provided that iterations converge. On the other hand, MFIE gives inaccurate results both in the near zone and in the far zone. Rate of occurrence of internal resonances increases at higher frequencies, while the effects of internal resonances spread around resonance frequencies. These make it impossible to use MFIE for electrically large objects. One well-known solution to the internal resonance problem is using CFIE, which is a linear combination of EFIE and MFIE. However, as discussed later, CFIE tends to possess the disadvantages of both EFIE and MFIE. Therefore, deriving a formulation that is only based on MFIE, while avoiding internal resonances and other disadvantages of this formulation, is always an attractive choice, as practiced in Chapter 4.

CHAPTER 2

ACCURATE TESTING OF THE MAGNETIC-FIELD INTEGRAL EQUATION

In this chapter, inaccuracy issues of MFIE are investigated with a particular focus on the selection of discretization functions. Possible discretization functions and their usage in the testing of MFIE are discussed. Then, the number of testing points is analyzed for the best accuracy and efficiency performance with MFIE. As shown via numerical examples, accuracy of MFIE can significantly be improved by a correct testing.

Applying Cauchy principal value integration, MFIE can be written as

$$\hat{\boldsymbol{n}} \times \mathcal{K}_{PV}\{\boldsymbol{J}\}(\boldsymbol{r}) + \Big(\frac{\Omega_0 - 4\pi}{4\pi}\Big)\boldsymbol{J}(\boldsymbol{r}) = -\hat{\boldsymbol{n}} \times \boldsymbol{H}^{inc}(\boldsymbol{r}), \tag{2.1}$$

where Ω_0 is the external solid angle at the observation point $\boldsymbol{r}$. By expanding the integro-differential operator, we can obtain

$$\hat{\boldsymbol{n}} \times \int_{\text{PV}} d\boldsymbol{r}' \boldsymbol{J}(\boldsymbol{r}') \times \nabla' g(\boldsymbol{r}, \boldsymbol{r}') + \Big(\frac{\Omega_0 - 4\pi}{4\pi}\Big)\boldsymbol{J}(\boldsymbol{r}) = -\hat{\boldsymbol{n}} \times \boldsymbol{H}^{inc}(\boldsymbol{r}), \tag{2.2}$$

where $g(\boldsymbol{r}, \boldsymbol{r}')$ is the free-space Green's function.

2.1 Error Sources in MFIE

It is known that, despite MFIE provides well-conditioned matrix equations and very fast iterative convergence rates, it leads to inaccurate results with the traditional discretization schemes. This inaccuracy further contaminates CFIE and leads to inaccurate results also with this popular formulation. Hence, several attempts have been conducted to obtain fast and accurate results with MFIE.

One of the early attempts to improve the accuracy of MFIE was on the efficient and reliable numerical calculation of the MFIE integrals by taking into account the $1/R^2$ singularity of the derivative of the Green's function in the integro-differential operator [1]. However, it was shown that, even if these integrals are handled carefully, MFIE is far worse than EFIE in terms of solution accuracy. Ubeda and Rius claimed that the inaccuracy of MFIE can be related to the selection of the solid angle factor and proposed an approximate formula for its correct estimation at the edges of triangulated geometries [2]. In 2004, Davis and Warnick applied a regularization to the identity operator to improve the accuracy of MFIE for the analysis of 2D objects [3]. They showed that the identity operator is the source of inaccurate results in spite of its trivial discretization and computation. However, the regularization of the identity operator could not be expanded easily for 3D objects and the inaccuracy due to the identity operator remained an unsolved issue. In the same year, Ergül and Gürel emphasized that the inaccuracy of MFIE is not related to the solid angle factor [4]. Studies by these authors and Ubeda et al. proposed careful selections of basis functions for better accuracy with MFIE [5, 6]. Ergül and Gürel further investigated the solid angle factor of MFIE [7] and showed that there is no need to estimate the solid angle and, using triangulated objects, it is sufficient to select the solid angle as 2π [7], which leads to the common form of MFIE as

$$\hat{\boldsymbol{n}} \times \boldsymbol{\mathcal{K}}_{PV}\{\boldsymbol{J}\}(\boldsymbol{r}) - \frac{1}{2}\boldsymbol{J}(\boldsymbol{r}) = -\hat{\boldsymbol{n}} \times \boldsymbol{H}^{inc}(\boldsymbol{r}) \tag{2.3a}$$

$$\hat{\boldsymbol{n}} \times \int_{\mathrm{PV}} d\boldsymbol{r}' \boldsymbol{J}(\boldsymbol{r}') \times \nabla' g(\boldsymbol{r}, \boldsymbol{r}') - \frac{1}{2}\boldsymbol{J}(\boldsymbol{r}) = -\hat{\boldsymbol{n}} \times \boldsymbol{H}^{inc}(\boldsymbol{r}). \tag{2.3b}$$

In 2005, Ergül and Gürel discussed the singularity of MFIE in detail along with various MFIE formulations and proposed a new singularity-extraction technique that provides accurate and efficient computation of the MFIE interactions [8]. Still, the accuracy of MFIE was not at the level of EFIE, after the improvements on singularity extraction techniques and proper selection of the solid angle factor [9]. Therefore, discussions regarding the accuracy improvement of MFIE continued on the selection of testing and basis functions [10–15].

2.2 Selection of Discretization Functions

By applying the method of moments on (2.3) using N basis and N testing functions ($\boldsymbol{b}_n(\boldsymbol{r})$ and $\boldsymbol{t}_m(\boldsymbol{r})$), the discretized form of the operators can be written as

$$\bar{\boldsymbol{K}}[m,n] = \int_{S_m} d\boldsymbol{r}\boldsymbol{t}_m(\boldsymbol{r}) \cdot \hat{\boldsymbol{n}} \times \int_{\mathrm{PV},S_n} d\boldsymbol{r}'\boldsymbol{b}_n(\boldsymbol{r}') \times \nabla' g(\boldsymbol{r},\boldsymbol{r}') \tag{2.4a}$$

$$\bar{\boldsymbol{I}}[m,n] = \int_{S_m} d\boldsymbol{r}\boldsymbol{t}_m(\boldsymbol{r}) \cdot \int_{S_n} d\boldsymbol{r}'\boldsymbol{b}_n(\boldsymbol{r}')\delta(\boldsymbol{r}-\boldsymbol{r}'). \tag{2.4b}$$

Matrix elements of MFIE can be then expressed in terms of the discretized operators as

$$\bar{\boldsymbol{Z}}[m,n] = \bar{\boldsymbol{K}}[m,n] - \frac{1}{2}\bar{\boldsymbol{I}}[m,n]. \tag{2.5}$$

The right-hand side of the formulation is obtained as

$$\boldsymbol{w}[m] = -\int_{S_m} d\boldsymbol{r}\boldsymbol{t}_m(\boldsymbol{r}) \cdot \hat{\boldsymbol{n}} \times \boldsymbol{H}^{inc}(\boldsymbol{r}). \tag{2.6}$$

In computational electromagnetics, basis functions used to expand the electric current density are often classified as divergence-conforming and curl-conforming functions. Divergence-conforming basis functions ensure the continuity of the normal component of the current density across the edges of triangles, while curl-conforming basis functions ensure the continuity of the tangential component.

A well-known discretization function set, Rao-Wilton-Glisson (RWG) functions [16] can be written as

$$\boldsymbol{b}_n^{\mathrm{RWG}}(\boldsymbol{r}) = \begin{cases} \dfrac{l_n}{2A_{n1}}(\boldsymbol{r}-\boldsymbol{r}_{n1}), & \boldsymbol{r} \in S_{n1} \\ \dfrac{l_n}{2A_{n2}}(\boldsymbol{r}_{n2}-\boldsymbol{r}), & \boldsymbol{r} \in S_{n2} \\ 0, & \boldsymbol{r} \notin S_n, \end{cases} \tag{2.7}$$

where l_n represents the length of the main edge, on which the function is defined, and A_{n1} and A_{n2} are respectively the areas of the first (S_{n1}) and second (S_{n2}) triangles associated with the edge. As a selected set, rotated RWG (rot-RWG) functions are obtained by simply rotating RWG functions using the triangle normals. It is well known that RWG functions are divergence conforming, while rot-RWG functions are

curl conforming. For example, the divergence of an RWG function can be written as

$$\nabla \cdot \boldsymbol{b}_n^{\mathrm{RWG}}(\boldsymbol{r}) = \begin{cases} \dfrac{l_n}{A_{n1}}, & \boldsymbol{r} \in S_{n1} \\ -\dfrac{l_n}{A_{n2}}, & \boldsymbol{r} \in S_{n2} \\ 0, & \boldsymbol{r} \notin S_n. \end{cases} \tag{2.8}$$

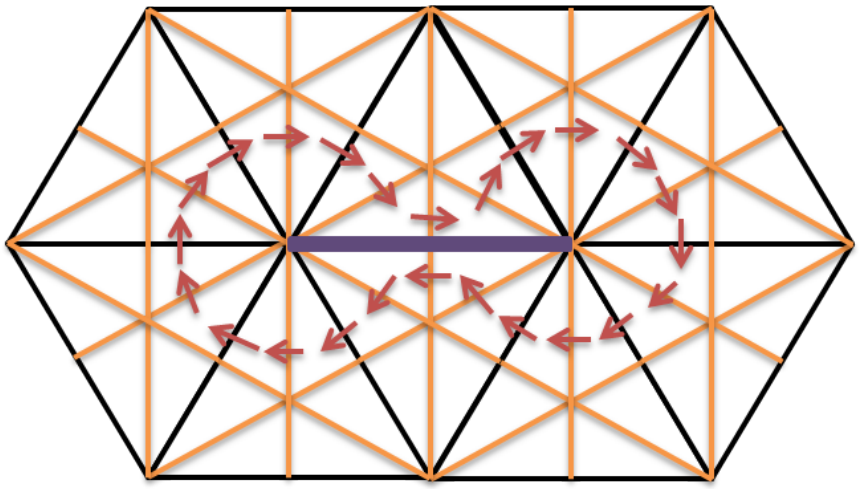

Figure 2.1: A Buffa-Christiansen function as a linear combination of the RWG functions defined on the barycentric mesh refinement.

Recently, Buffa-Christiansen (BC) functions [17] were introduced as a new set of divergence-conforming functions. BC functions, like RWG functions, are defined on the main edges of the triangulated geometries. For a selected edge, the BC function is a linear combination of the RWG functions defined on the barycentrically refined mesh around the edge (see Figure 2.1). For the sake of simplicity, RWG functions used to define BC functions are named as sub-RWG functions. The definition of a sub-RWG function is the same as the definition of an RWG function given in (2.7).

In Figure 2.1, the main mesh of the geometry is shown with black lines, while barycentrically refined mesh is shown with yellow lines. To define a BC function on the purple edge, the nodes of the edge are taken into account. The BC function is a linear combination of all sub-RWG functions, shown with red arrows, connected to these nodes besides the ones on the main edge. Moreover, rotated BC (rot-BC) functions are defined by rotating each sub-RWG function using the normal vectors of their triangles.

In order to discretize MFIE, studies in the literature mainly focus on the Galerkin discretization scheme based on using the same discretization elements for both basis and testing functions. In addition to RWG and BC functions, linear-linear basis functions are also used to discretize MFIE, as well as CFIE [15]. Also, mono-polar RWG functions that use different expansion coefficients for half RWG functions can be employed to discretize MFIE [11]. The improved accuracy obtained with the mono-polar functions clearly demonstrate that the standard RWG functions are insufficient for MFIE especially for objects with sharp edges. Ergül and Gürel showed that using rot-RWG functions as basis functions leads to better accuracy for MFIE [12], which is later extended to linear-linear functions for significantly accurate results [13, 15]. However, it has been shown that the inaccuracy is related to the inaccurate testing of MFIE, and Galerkin discretization scheme is simply not suitable for this integral equation [18–22].

2.3 Testing of Identity Operator

Although it is a trivial operator to calculate numerically, the identity operator is the main source of the inaccuracy in the conventional discretizations of MFIE [23], and this is mainly related to the testing of this integral equation. To understand this, we first note that the divergence and curl operators can be seen as dual of each other. Therefore, function spaces of divergence-conforming and curl-conforming functions can be considered to be dual spaces. Furthermore, using integral equations, an operator needs to be tested in the dual space of its range [18]. In this context, we may focus on four different types of functions, namely RWG, rot-RWG, BC, and rot-BC functions. Among these, RWG and BC functions constitute divergence-conforming function spaces, while rot-RWG and rot-BC functions constitute curl-conforming function spaces. The spaces of RWG (or BC) and rot-RWG (or rot-BC) functions are dual spaces of each other.

The identity operator dominates MFIE, so it can be taken into account when we consider the range space of MFIE. When the identity operator is applied on the functions, the ranges for RWG and BC basis functions are divergence-conforming function spaces, while they are curl-conforming function spaces for rot-RWG and rot-BC

functions. Then, by the principle of testing with the dual space of the range, it is required to test the operator with curl-conforming functions when the current density is expanded with divergence-conforming functions, and vice versa.

If the current density is expanded with RWG basis functions there are two possibilities to test the identity operator, i.e. testing with rot-RWG or rot-BC functions, considering correct spaces. However, if RWG basis functions are tested with rot-RWG testing functions, the diagonal elements are tested weakly as

$$\bar{\boldsymbol{I}}[m,m] = \int_{S_m} d\boldsymbol{r}(\hat{\boldsymbol{n}} \times \boldsymbol{f}_m^{\mathrm{RWG}}(\boldsymbol{r})) \cdot \boldsymbol{f}_m^{\mathrm{RWG}}(\boldsymbol{r}) = 0 \tag{2.9}$$

due to the orthogonality of RWG and rot-RWG functions. Consequently, when the electric current density is expanded with RWG functions, the best set to test the identity operator is rot-BC functions since these functions are pseudo divergence conforming and they lead to well-tested identity operator. This is called a mixed discretization scheme [18, 19].

As numerical examples, a sphere with a radius of 0.3 m is analyzed by applying Galerkin and mixed discretization schemes to MFIE. For the Galerkin discretization, RWG functions are selected as discretization (both testing and basis) functions. On the other hand, RWG functions are selected as basis functions and rot-BC functions are selected as testing functions for the mixed discretization scheme. Therefore, only the testing scheme (but not the expansion of the current density) is tested. Numerical computations of the test integrals are performed via single-point testing. Generalized minimal residual method (GMRES) is used as the iterative solver of the constructed matrix equations, while matrix-vector multiplications are accelerated by using the multilevel fast multipole algorithm (MLFMA) [24]. The sphere, which is discretized with 20 mm triangles, is investigated in a frequency range between 0.5 GHz and 1.2 GHz with a step size of 10 MHz. The excitation is a linearly polarized plane wave with $+z$ propagation and $+x$ polarization.

In Figure 2.2, normalized backscattered RCS values (RCS$/\pi a^2$, where a is the radius of the sphere) are plotted in the selected frequency range. In addition to numerical results obtained by using RWG and rot-BC testing functions, analytical Mie-series results are plotted (black line) as reference values. In all simulations, the relative

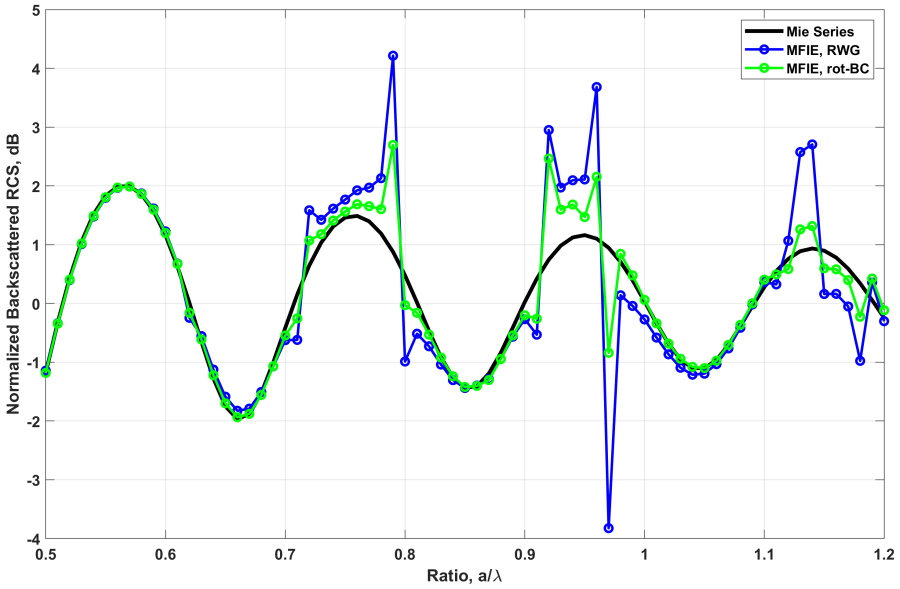

Figure 2.2: Normalized backscattered RCS of a sphere with $a = 0.3$ m radius from 0.5 GHz to 1.2 GHz. The numerical results are obtained by using MFIE discretized with RWG and rot-BC testing functions.

error is defined as

$$\text{Relative Error} = \frac{||\boldsymbol{E}_c^{\infty} - \boldsymbol{E}_a^{\infty}||_2}{||\boldsymbol{E}_a^{\infty}||_2}, \tag{2.10}$$

where $\boldsymbol{E}_a^{\infty}$ and $\boldsymbol{E}_c^{\infty}$ correspond to the analytically and computationally computed far-zone electric field intensity vectors, respectively, on the E-plane with 360 sample points. The relative errors in numerically computed electric field intensity values in the far-zone E-plane are also computed (with respect to the analytical solutions) and shown in Figure 2.3. The internal resonance problem of MFIE can be identified at around 0.8 GHz, 0.95 GHz, and 1.15 GHz. Specifically, at these resonance frequencies, the numerical field values diverge from the analytical solutions and the error increases dramatically as observed in Figure 2.3. In Figure 2.4, the required numbers of iterations are plotted with respect to frequency. It can be observed that the number of iterations tends to increase at resonance frequencies for both RWG and rot-BC testing. In general, using rot-BC functions does not eliminate the internal resonances of MFIE. But, these functions clearly improve the accuracy considering the solutions between the resonances. It is remarkable that rot-BC functions lead to better-conditioned matrix equations, while this is mostly related to the overall number

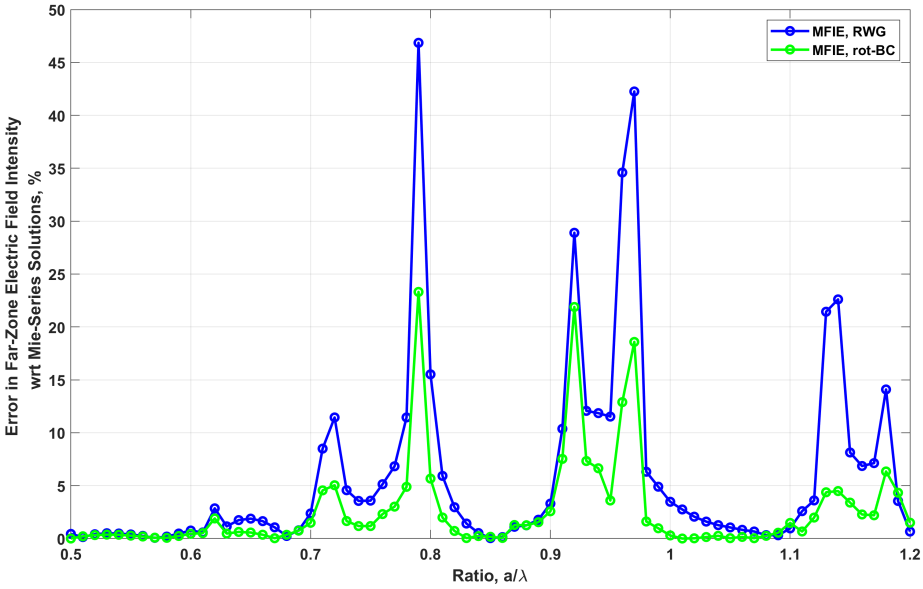

Figure 2.3: The relative error in the far-zone electric field intensity with respect to Mie-series solutions of a sphere with 0.3 m radius from 0.5 GHz to 1.2 GHz. The numerical results are obtained by using MFIE discretized with RWG and rot-BC testing functions.

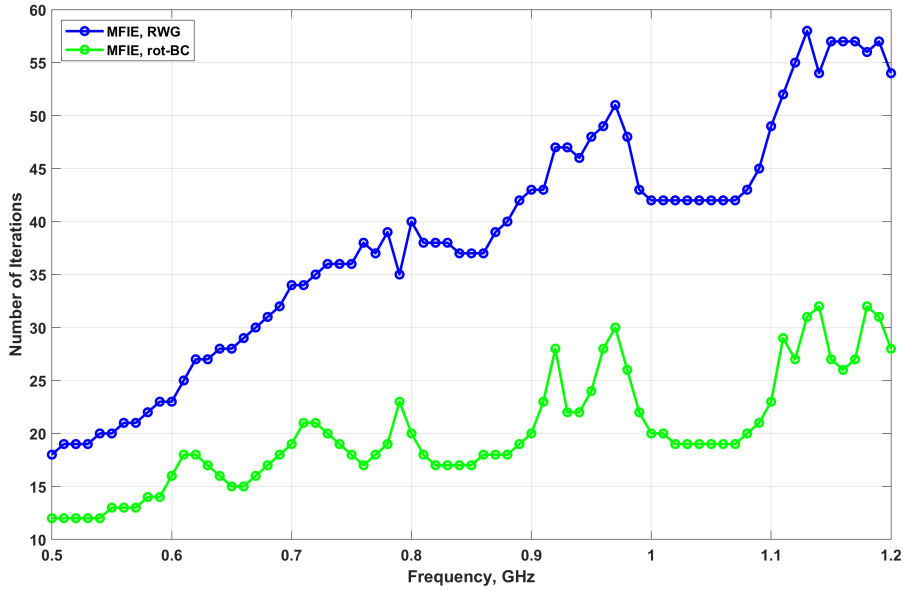

Figure 2.4: Numbers of iterations required for the analysis of a sphere with 0.3 m radius from 0.5 GHz to 1.2 GHz. The numerical results are obtained by using MFIE discretized with RWG and rot-BC testing functions.

of testing points, as shown in the next section.

2.4 Number of Testing Points

The number of quadrature points used to evaluate testing integrals directly affects the accuracy of MFIE. Two types of possible functions that can be used to expand the current density are RWG and BC functions. Both of these functions are first-order polynomial vector functions. When these functions are used for the identity operator, the term inside the interaction integral is a second-order polynomial. Then, the numerical computation of the identity operator using the three-point Gaussian quadrature rule can be as accurate as its analytical calculation.

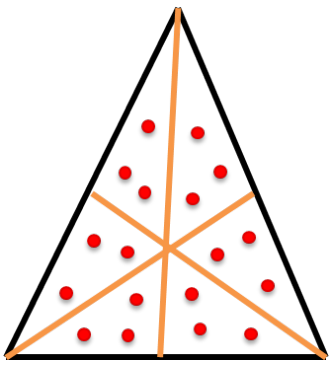

Figure 2.5: Three-point testing locations (shown with red dots) for sub-triangles (shown with orange lines) of a barycentrically refined triangle (the black line).

Another consideration about testing points is the increased numbers of samples when using rot-BC functions for MFIE. As shown in Figure 2.5, a triangle is divided into six sub-triangles when a barycentric mesh refinement is applied. Then, a total of eighteen points are effectively used for the master triangle when each sub-triangle is sampled at three points. Therefore, testing with rot-BC functions with the three-point Gaussian quadrature is equivalent to testing with RWG functions with eighteen points per triangle.

In order to demonstrate the effect of the number of testing points on the accuracy and conditioning of MFIE, analysis of a sphere with 0.3 m radius is considered with increasing numbers of testing points. Testing at a single point, as well as at three

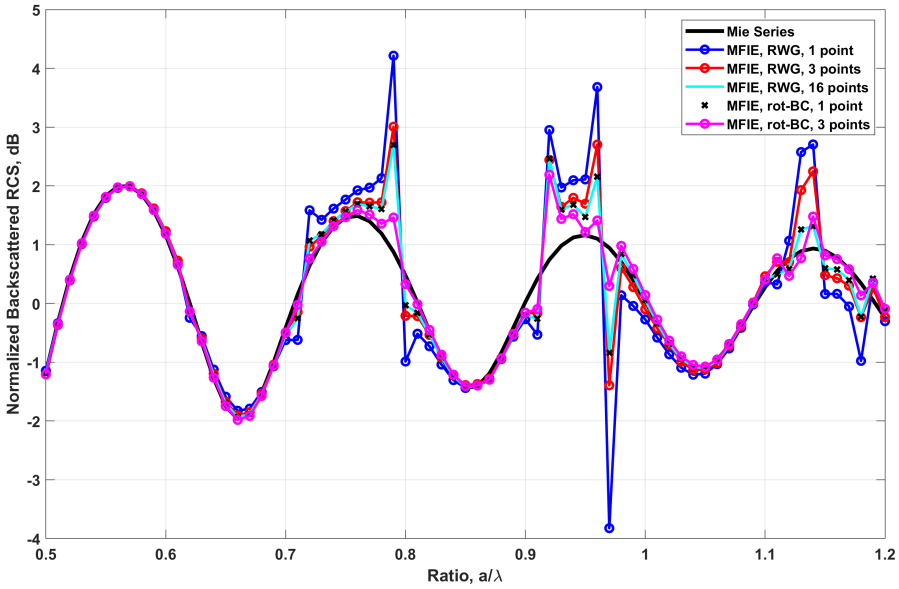

Figure 2.6: Normalized backscattered RCS of a sphere with $a = 0.3$ m radius from 0.5 GHz to 1.2 GHz. The results are obtained with different numbers of testing points for RWG and rot-BC testing functions.

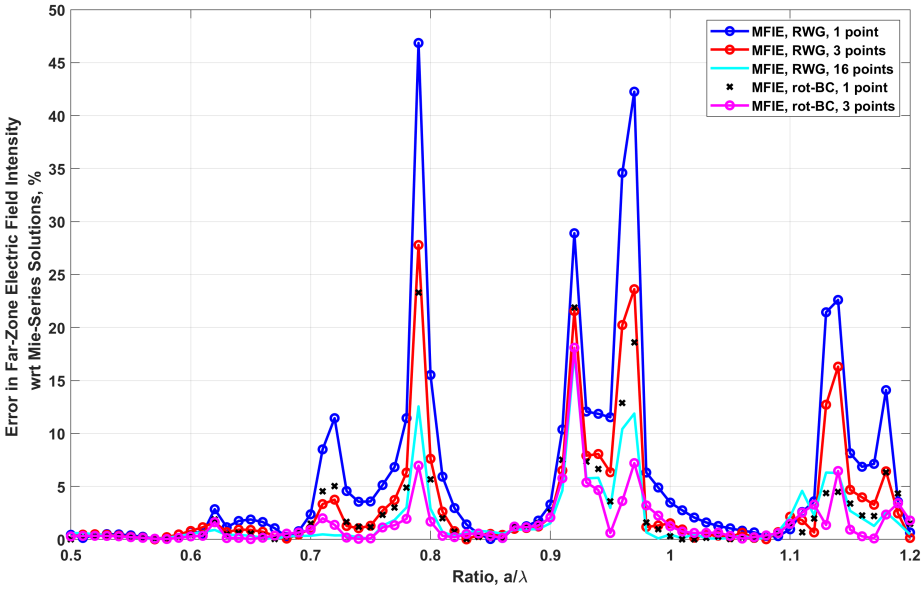

Figure 2.7: The relative error in the far-zone electric field intensity with respect to Mie-series solutions of a sphere with 0.3 m radius from 0.5 GHz to 1.2 GHz. The results are obtained with different numbers of testing points for RWG and rot-BC testing functions.

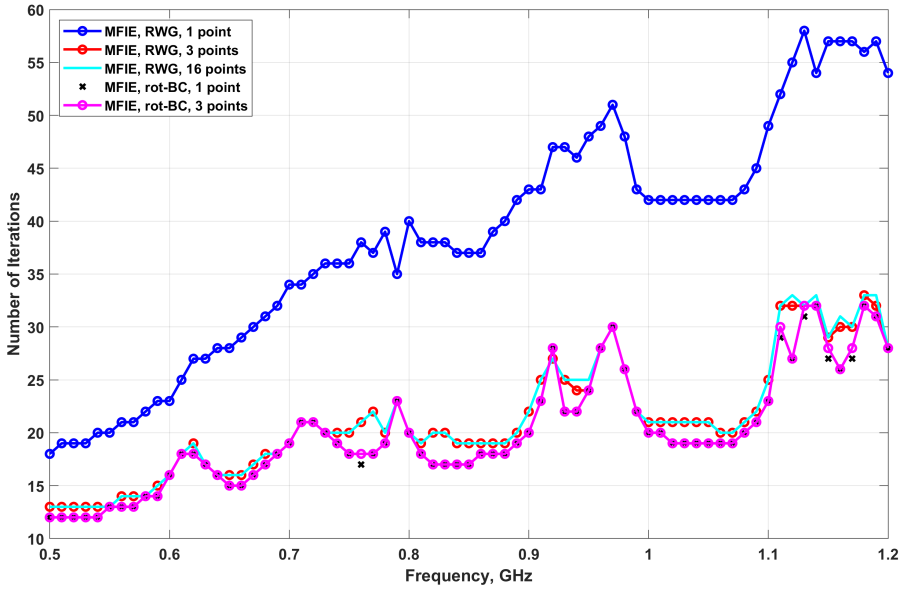

Figure 2.8: Numbers of iterations required for the analysis of a sphere with 0.3 m radius from 0.5 GHz to 1.2 GHz.

and sixteen points per triangle are considered for the Galerkin discretization scheme (RWG testing functions), while testing at a single point and at three points are considered for the mixed discretization scheme (rot-BC testing functions). The normalized backscattered RCS, the relative error in the far-zone scattered field, and the number of iterations are depicted in Figures 2.6, 2.7, and 2.8, respectively, in the frequency range between 0.5 GHz and 1.5 GHz with a step size of 10 MHz. In Figures 2.6 and 2.7, it can be observed that accuracy of MFIE dramatically improves with increasing numbers of test points for both discretization schemes. Obviously, increasing the number of testing points does not solve the internal-resonance problem although it increases the quality factors of the resonances. The latter is due to the fact that the nature of the internal-resonance problem is based on the formulation and not on the discretization scheme. More importantly, testing with rot-BC functions gives better accuracy than testing with RWG functions regardless of the number of test points. For example, better accuracy is obtained by testing with rot-BC functions using three points (per sub-triangle) rather than testing with RWG functions using sixteen points (per triangle). This means that the accuracy improvement is related to the correct selection of the test functions rather than the number of sampling points. In Figure 2.8, it can be

observed that testing by using three points per master triangle (i.e., results other than single-point testing with RWG functions) leads to fast convergence for both RWG and rot-BC testing functions. Overall, it can be said that the best results in terms of accuracy and iterative convergence are obtained by testing with rot-BC functions and three points per sub-triangle when expanding the electric current density with RWG functions. Although not shown, further increasing the number of samples for rot-BC functions does not significantly improve the accuracy and conditioning, while it increases the processing time.

2.5 Concluding Remarks

MFIE provides well-conditioned matrix equations and very fast iterative convergence rates, but it leads to inaccurate results with the traditional discretization schemes. The accuracy of MFIE does not reach the accuracy of EFIE, after many improvements on singularity extraction techniques and proper selection of the solid angle factor. In addition, it was shown that the identity operator is the main source of the inaccuracy of MFIE, although it is a trivial operator to calculate numerically. Therefore, discussions in the literature on the accuracy of MFIE have focused on the selection of testing and basis functions, particularly on the correct testing of the identity operator (hence MFIE).

As discussed in this chapter, the inaccuracy of MFIE is related to the inaccurate testing of this formulation, and Galerkin discretization scheme is simply not suitable for MFIE. By the principle of testing with the dual space of the range, it is required to test the identity operator with curl-conforming functions when the current density is expanded with divergence-conforming functions, and vice versa. Consequently, when the electric current density is expanded with RWG functions, an ideal set to test the identity operator is rot-BC functions since these functions are not only curl conforming but also pseudo divergence conforming, leading to well-tested identity operator. This is called a mixed discretization scheme in the literature. Using rot-BC functions does not eliminate internal resonances of MFIE, but they clearly improve the accuracy considering the solutions between resonances.

Finally, as also shown in numerical examples, the accuracy improvement provided by rot-BC functions is related to the correct selection of the testing function space rather than the increased number of sampling points. The results show that the best results in terms of accuracy and iterative convergence are obtained by testing with rot-BC functions and three points per sub-triangle when expanding the electric current density with RWG functions.

CHAPTER 3

MIXED DISCRETIZATION OF THE COMBINED-FIELD INTEGRAL EQUATION

The inaccuracy of MFIE at non-resonant frequencies can be mitigated by using a correct testing with a mixed discretization scheme employing RWG functions as basis and rot-BC functions for testing, as described in Chapter 2. Since the inaccuracy of MFIE contaminates CFIE [25], the same mixed discretization scheme can be used to improve the accuracy of CFIE. On the other hand, when extending the use of BC functions to CFIE, i.e., using BC functions for testing MFIE and using RWG functions for testing EFIE, a direct convex combination does not eliminate internal resonances. To solve this problem, projection of testing spaces onto each other is required, which can be achieved via Gram matrices involving the inner products of RWG and BC functions.

In this chapter, discretization of CFIE is firstly discussed. Requirement of projection of testing spaces for the mixed discretization scheme is shown with numerical examples. The effect of the CFIE factor on the solution accuracy and convergence rate is also shown. Finally, inversion of gram matrices in mixed CFIE is discussed in the context of MLFMA.

3.1 Discretization of CFIE

$N \times N$ matrix equations obtained by the application of the method of moments via a set of basis and testing functions can be written in the form of

$$\bar{\boldsymbol{Z}} \cdot \boldsymbol{a} = \boldsymbol{w}. \tag{3.1}$$

Using RWG basis functions, the matrix elements for EFIE can be written as

$$\bar{\boldsymbol{Z}}^{\text{EFIE}}[m,n] = i\omega\mu \int_{S_m} d\boldsymbol{r}\boldsymbol{t}_m(\boldsymbol{r}) \cdot \int_{S_n} d\boldsymbol{r}' \boldsymbol{f}_n^{\text{RWG}}(\boldsymbol{r}')g(\boldsymbol{r},\boldsymbol{r}') + \frac{1}{i\omega\epsilon} \int_{S_m} d\boldsymbol{r}\nabla \cdot \boldsymbol{t}_m(\boldsymbol{r}) \int_{S_n} d\boldsymbol{r}' g(\boldsymbol{r},\boldsymbol{r}')\nabla' \cdot \boldsymbol{f}_n^{\text{RWG}}(\boldsymbol{r}'), \tag{3.2}$$

while the matrix elements for MFIE can be written as

$$\bar{\boldsymbol{Z}}^{\text{MFIE}}[m,n] = -\frac{1}{2} \int_{S_m} d\boldsymbol{r}\boldsymbol{t}_m(\boldsymbol{r}) \cdot \boldsymbol{f}_n^{\text{RWG}}(\boldsymbol{r}) + \int_{S_m} d\boldsymbol{r}\boldsymbol{t}_m(\boldsymbol{r}) \cdot \hat{\boldsymbol{n}} \times \int_{\text{PV},S_n} d\boldsymbol{r}' \boldsymbol{f}_n^{\text{RWG}}(\boldsymbol{r}') \times \nabla' g(\boldsymbol{r},\boldsymbol{r}'). \tag{3.3}$$

Also, the right-hand-side elements for EFIE can be written as

$$\boldsymbol{w}^{\text{EFIE}}[m] = -\int_{S_m} d\boldsymbol{r}\boldsymbol{t}_m(\boldsymbol{r}) \cdot \boldsymbol{E}^{\text{inc}}(\boldsymbol{r}), \tag{3.4}$$

while they can be written as

$$\boldsymbol{w}^{\text{MFIE}}[m] = -\int_{S_m} d\boldsymbol{r}\boldsymbol{t}_m(\boldsymbol{r}) \cdot \hat{\boldsymbol{n}} \times \boldsymbol{H}^{\text{inc}}(\boldsymbol{r}) \tag{3.5}$$

for MFIE. In the given equations, $\boldsymbol{f}_n^{\text{RWG}}$ represents RWG functions defined for $n = 1, 2, ..., N$, while $\boldsymbol{t}_m$ represents the testing functions for $m = 1, 2, ..., N$. In this work, RWG functions and rot-BC functions are used as testing functions for EFIE and MFIE, respectively.

In general, CFIE is linear convex combination of MFIE and EFIE. The matrix elements for CFIE can be written as

$$\bar{\boldsymbol{Z}}^{\text{CFIE}} = \alpha\bar{\boldsymbol{Z}}^{\text{EFIE}} + (1-\alpha)\eta\bar{\boldsymbol{Z}}^{\text{MFIE}}, \tag{3.6}$$

while the corresponding right-hand-side vector can be written as

$$\boldsymbol{w}^{\text{CFIE}} = \alpha\boldsymbol{w}^{\text{EFIE}} + (1-\alpha)\eta\boldsymbol{w}^{\text{MFIE}}. \tag{3.7}$$

In (3.6) and (3.7), α represents the combination ratio of EFIE and MFIE, while η represents the free-space intrinsic impedance. α is selected as 0.5 for all CFIE variations in this work.

As a numerical example, a sphere with a radius of 0.3 m is analyzed iteratively using GMRES. The solutions are obtained for a frequency range between 0.5 GHz and 1.2 GHz with a step size of 10 MHz. For the solution with CFIE, RWG functions are

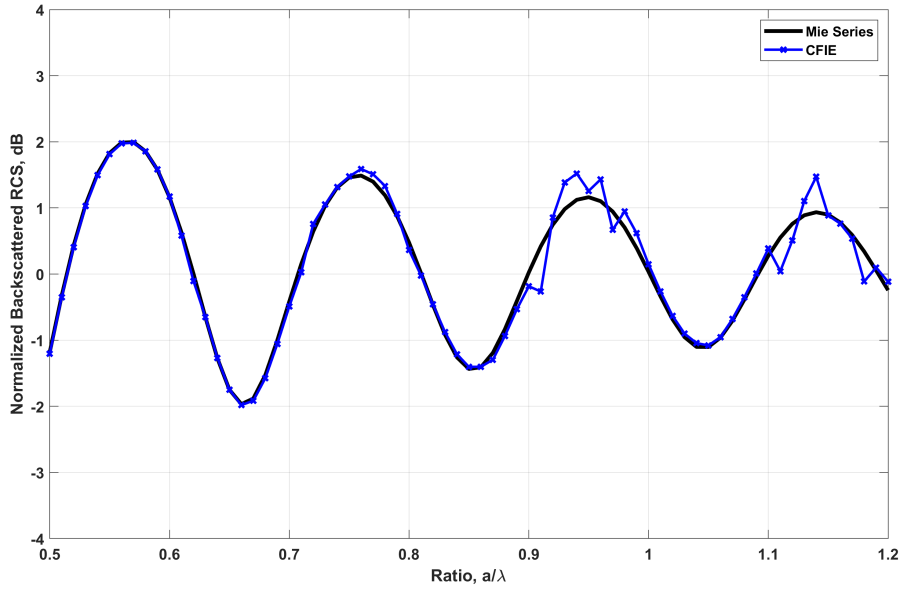

Figure 3.1: Normalized backscattered RCS with respect to Mie-series solutions of a sphere with 0.3 m radius from 0.5 GHz to 1.2 GHz. The results are obtained with CFIE with mixed discretizations when EFIE and MFIE are combined directly (convex combination).

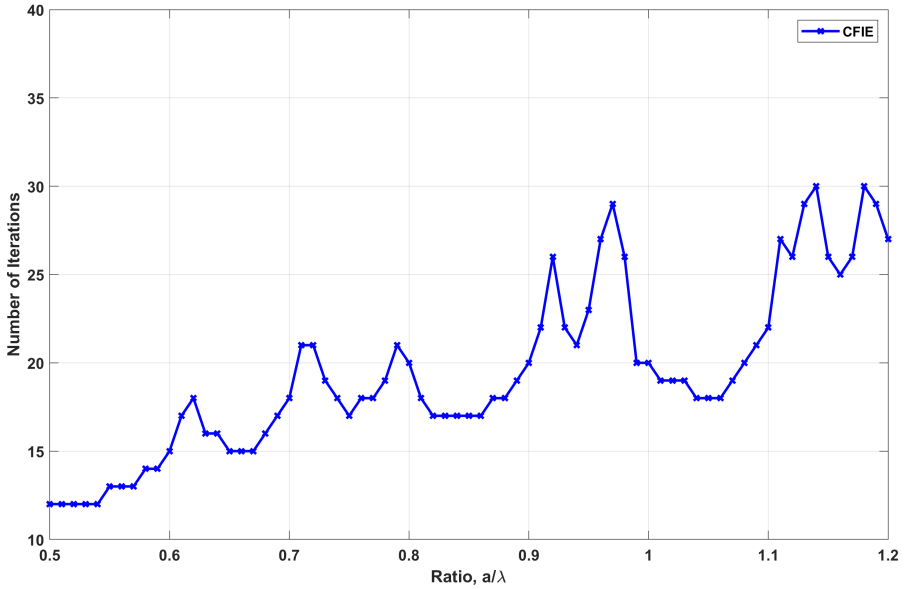

Figure 3.2: Numbers of iterations for the analysis of a sphere with 0.3 m radius from 0.5 GHz to 1.2 GHz. The results are obtained with CFIE with mixed discretizations when EFIE and MFIE are combined directly (convex combination).

used as basis functions. As testing functions, rot-BC functions are used for the MFIE part while RWG functions are used for the EFIE part. As it is well-known in the literature, EFIE is well-tested when the Galerkin scheme is used; therefore, its discretization functions are selected as RWG functions. The normalized backscattered RCS values and the corresponding numbers of iterations are given in Figures 3.1 and 3.2, respectively. In Figure 3.1, it can be observed that there are inaccuracy problems at the resonance frequencies of MFIE, even though CFIE is used. Moreover, Figure 3.2 shows that the number of iterations is not stable as one would expect from CFIE. These results show that the well-known CFIE formulation given in (3.6) and (3.7) is not suitable to be solved via the mixed discretization scheme (with direct combination of EFIE and MFIE) that is essential for accurate results with MFIE.

In order to mitigate the internal resonance problem using CFIE, both EFIE and MFIE are required to be tested with the functions in the same testing space. When MFIE is tested with rot-BC functions and EFIE is tested with RWG functions, the reflection of testing spaces onto each other is required [26]. In this case, CFIE can be written as

$$\bar{\boldsymbol{Z}}^{\text{CFIE}} = \alpha \bar{\boldsymbol{Z}}^{\text{EFIE}} + (1-\alpha)\eta \bar{\boldsymbol{G}}_{\text{RWG,RWG}} \cdot [\bar{\boldsymbol{G}}_{n\times\text{BC,RWG}}]^{-1} \cdot \bar{\boldsymbol{Z}}^{\text{MFIE}} \tag{3.8}$$

or

$$\bar{\boldsymbol{Z}}^{\text{CFIE}} = \alpha \bar{\boldsymbol{G}}_{n\times\text{BC,RWG}} \cdot [\bar{\boldsymbol{G}}_{\text{RWG,RWG}}]^{-1} \cdot \bar{\boldsymbol{Z}}^{\text{EFIE}} + (1-\alpha)\eta \bar{\boldsymbol{Z}}^{\text{MFIE}}, \tag{3.9}$$

where $\bar{\boldsymbol{G}}_{n\times\text{BC,RWG}}$ represents the Gram matrix that includes the inner products of RWG and rot-BC functions, while $\bar{\boldsymbol{G}}_{\text{RWG,RWG}}$ represents the Gram matrix that contains inner products of RWG functions. In addition, the corresponding right-hand-side vectors can be written as

$$\boldsymbol{w}^{\text{CFIE}} = \alpha \boldsymbol{w}^{\text{EFIE}} + (1-\alpha)\eta \bar{\boldsymbol{G}}_{\text{RWG,RWG}} \cdot [\bar{\boldsymbol{G}}_{n\times\text{BC,RWG}}]^{-1} \cdot \boldsymbol{w}^{\text{MFIE}} \tag{3.10}$$

and

$$\boldsymbol{w}^{\text{CFIE}} = \alpha \bar{\boldsymbol{G}}_{n\times\text{BC,RWG}} \cdot [\bar{\boldsymbol{G}}_{\text{RWG,RWG}}]^{-1} \cdot \boldsymbol{w}^{\text{EFIE}} + (1-\alpha)\eta \boldsymbol{w}^{\text{MFIE}}, \tag{3.11}$$

respectively. In this work, (3.9) is used together with (3.11) to obtain the numerical results. In order to demonstrate the developed CFIE based on (3.9) and (3.11), the previous sphere problems are analyzed again. In Figure 3.3, it can be observed that the results obtained with the mixed CFIE using the reflection of testing spaces closely

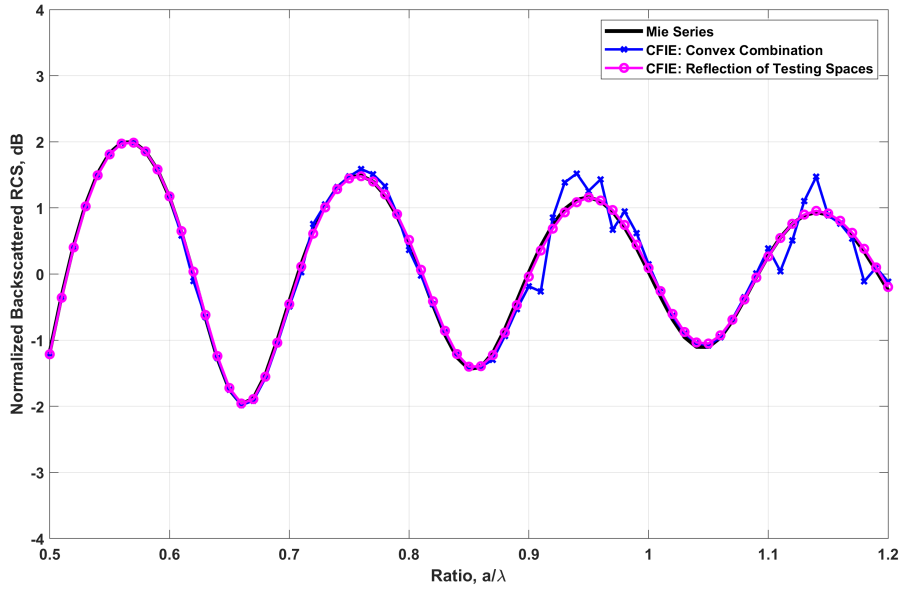

Figure 3.3: Normalized backscattered RCS with respect to Mie-series solutions of a sphere with a radius of 0.3 m from 0.5 GHz to 1.2 GHz. The results are obtained by using CFIE with mixed discretizations when EFIE and MFIE are combined directly (convex combination) and via reflection of testing spaces.

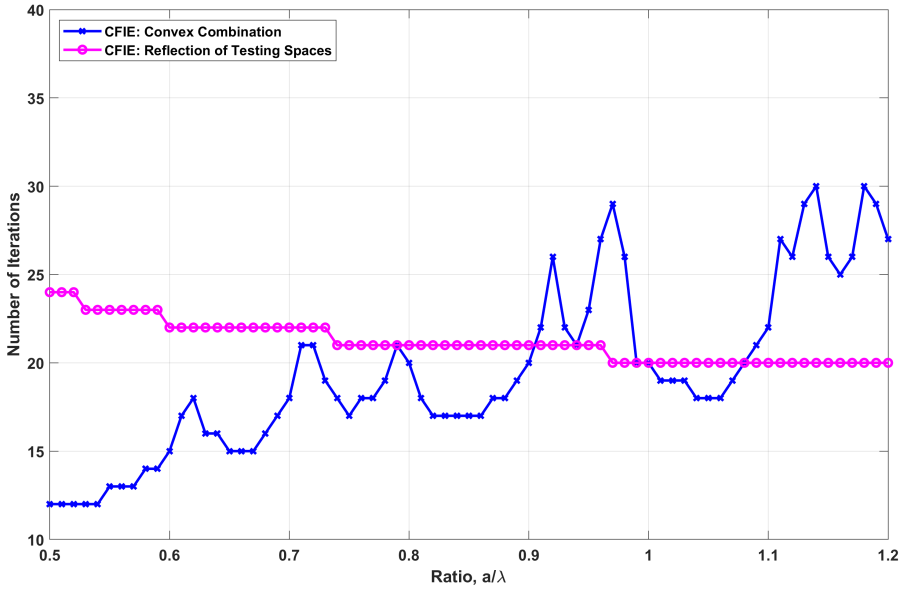

Figure 3.4: Numbers of iterations for the analysis of a sphere with 0.3 m radius from 0.5 GHz to 1.2 GHz. The results are obtained by using CFIE with mixed discretizations when EFIE and MFIE are combined directly (convex combination) and via reflection of testing spaces.

follows the Mie series solutions of the sphere. In addition, as shown in Figure 3.4, the number of iterations is steady as expected for a CFIE formulation. These results clearly show that the reflection of testing spaces with Gram matrices is essential when a mixed discretization is used for CFIE.

3.2 Effect of Mixed Discretization on the CFIE Factor

CFIE factor (α) is a parameter that defines the weights of EFIE and MFIE in the combined formulation. As α goes to one (zero), CFIE converges into EFIE (MFIE). As it is well-known that EFIE gives accurate results with large numbers of iterations while MFIE gives relatively inaccurate results with small numbers of iterations, we need to select α carefully with the consideration of the trade-off between the number of iterations and accuracy. For the classic implementation of CFIE with a Galerkin discretization scheme, a suitable value of α is considered to be 0.2. However, the optimal value naturally changes depending on the discretization strategy. In this work, the optimal CFIE factor in the context of its mixed discretization is investigated.

As an example, a sphere with a radius of 0.3 m is analyzed at 1.05 GHz. The sphere is discretized with 20 mm triangles that leads to 9414 unknowns. The value of α is swept from 0 to 1 for both Galerkin and mixed discretization schemes. Testing integrals are computed by using three points per triangle as suggested in Chapter 2. In Figures 3.5 and 3.6, the far-field error in the E-plane with respect to the analytical Mie-series solutions and the corresponding numbers of iterations can be observed for different values of α. In these figures, it is observed that the CFIE with the mixed discretization provides better accuracy and iterative convergence than the one with the Galerkin discretization scheme. In the case of the analysis of a sphere, 0.35 can be selected for the best convergence rate and good accuracy. It is interesting to observe that α values around 0.1 provides solutions with extremely small errors.

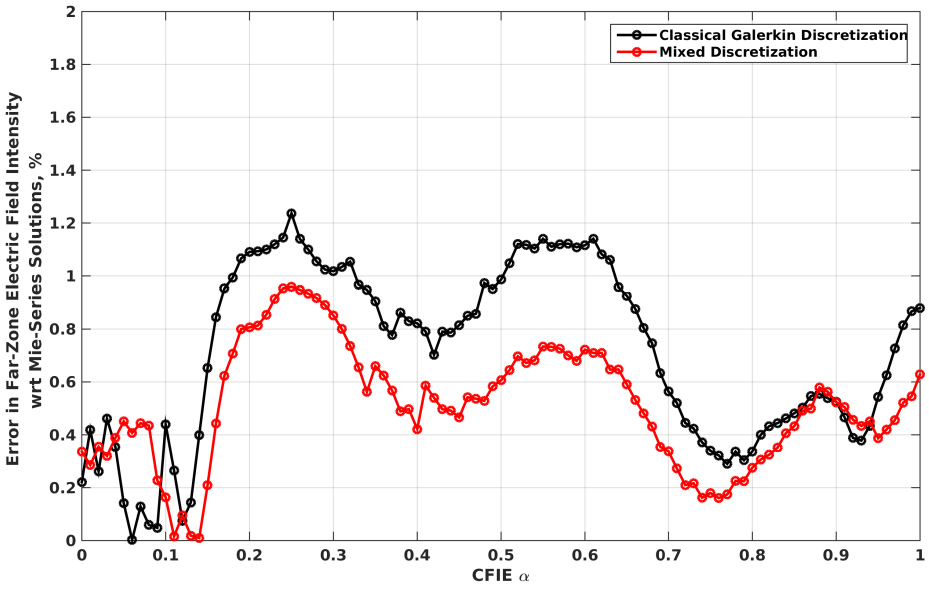

Figure 3.5: Relative error in the far-zone electric field intensity obtained in the analysis of a sphere with 0.3 m radius at 1.05 GHz. Solutions are obtained by using CFIE discretized with Galerkin and mixed discretization schemes and the numerical values are compared against Mie-series solutions.

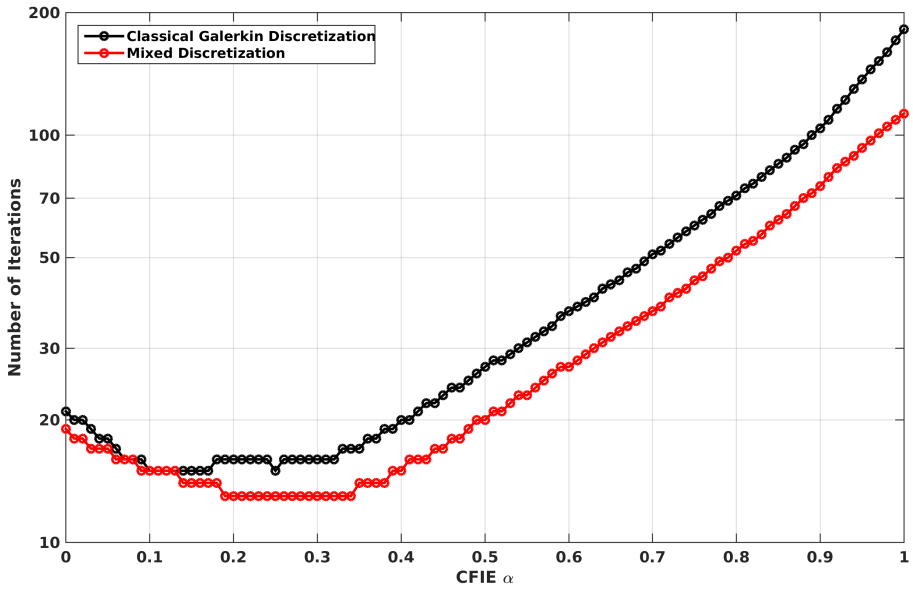

Figure 3.6: Numbers of iterations required for the analysis of a sphere with 0.3 m radius at 1.05 GHz. Solutions are obtained by using CFIE discretized with Galerkin and mixed discretization schemes.

3.3 Mixed CFIE for Large Problems

In the analysis of electrically large problems, MLFMA can be used as an accelerator for the matrix-vector multiplications required by the iterative solvers. It is well-known that MLFMA operates with $O(N \log N)$ complexity. However, inversions of Gram matrices are required in the proposed formulations in (3.8) and (3.9), which generally require $O(N^3)$ processing times. Therefore, it is required to accelerate the inversions of Gram matrices to use the mixed CFIE formulation for electrically large objects.

In this work, matrix inversion techniques are compared in terms of accuracy and efficiency in the context of inversion of Gram matrices. The first of them is the LU factorization that can be written as $\bar{\boldsymbol{P}} \cdot [\bar{\boldsymbol{R}}^{-1} \cdot \bar{\boldsymbol{A}}] \cdot \bar{\boldsymbol{Q}} = \bar{\boldsymbol{L}} \cdot \bar{\boldsymbol{U}}$, where $\bar{\boldsymbol{P}}$ and $\bar{\boldsymbol{Q}}$ represent permutation matrices, $\bar{\boldsymbol{R}}$ represents diagonal scaling matrix, $\bar{\boldsymbol{L}}$ represents lower triangular matrix, and $\bar{\boldsymbol{U}}$ represents upper triangular matrix for a given system matrix $\bar{\boldsymbol{A}}$. Using the LU factorization, the inverse of matrix $\bar{\boldsymbol{A}}$ can be written as

$$\bar{\boldsymbol{A}}^{-1} = \bar{\boldsymbol{Q}} \cdot \left[\bar{\boldsymbol{U}}^{-1} \cdot [\bar{\boldsymbol{L}}^{-1} \cdot (\bar{\boldsymbol{P}} \cdot \bar{\boldsymbol{R}}^{-1})]\right]. \tag{3.12}$$

The second one is LDLT factorization that can be written as $\bar{\boldsymbol{P}}^{\mathrm{H}} \cdot \bar{\boldsymbol{S}} \cdot \bar{\boldsymbol{A}} \cdot \bar{\boldsymbol{S}} \cdot \bar{\boldsymbol{P}} = \bar{\boldsymbol{L}} \cdot \bar{\boldsymbol{D}} \cdot \bar{\boldsymbol{L}}^{\mathrm{H}}$, where $\bar{\boldsymbol{L}}$ represents lower triangular matrix, $\bar{\boldsymbol{D}}$ represents diagonal matrix, $\bar{\boldsymbol{P}}$ represents permutation matrix, and $\bar{\boldsymbol{S}}$ represents scaling matrix for a given matrix $\bar{\boldsymbol{A}}$. Then, the inverse of matrix $\bar{\boldsymbol{A}}$ can be written as

$$\bar{\boldsymbol{A}}^{-1} = \bar{\boldsymbol{S}} \cdot \bar{\boldsymbol{P}} \cdot \left[(\bar{\boldsymbol{L}}^{\mathrm{H}})^{-1} \cdot \left[\bar{\boldsymbol{D}}^{-1} \cdot \left(\bar{\boldsymbol{L}}^{-1} \cdot (\bar{\boldsymbol{P}}^{\mathrm{H}} \cdot \bar{\boldsymbol{S}})\right)\right]\right]. \tag{3.13}$$

In the above, superscript H represents the Hermitian operator. The third one is Cholesky factorization that can be written as $\bar{\boldsymbol{L}} \cdot \bar{\boldsymbol{L}}^{\mathrm{H}} = \bar{\boldsymbol{P}}^{\mathrm{H}} \cdot \bar{\boldsymbol{A}} \cdot \bar{\boldsymbol{P}}$, where $\bar{\boldsymbol{L}}$ represents lower triangular matrix and $\bar{\boldsymbol{P}}$ represents permutation matrix. Using this factorization, the inverse of matrix $\bar{\boldsymbol{A}}$ can be written as

$$\bar{\boldsymbol{A}}^{-1} = \bar{\boldsymbol{P}} \cdot \left[(\bar{\boldsymbol{L}}^{\mathrm{H}})^{-1} \cdot (\bar{\boldsymbol{L}}^{-1} \cdot \bar{\boldsymbol{P}}^{\mathrm{H}})\right]. \tag{3.14}$$

Besides the factorization techniques, iterative solvers can be used to compute inverse matrix-vector multiplication for a known matrix. Specifically, to perform multiplication $\bar{\boldsymbol{A}}^{-1} \cdot \boldsymbol{x}$, equation $\bar{\boldsymbol{A}} \cdot \boldsymbol{u} = \boldsymbol{x}$ can be solved iteratively to obtain $\boldsymbol{u}$ as the result.

In the following, a sphere with a radius of 0.3 m is used to compare the described methods. The mesh size is selected with the rule of thumb as $\lambda/10$, while the number

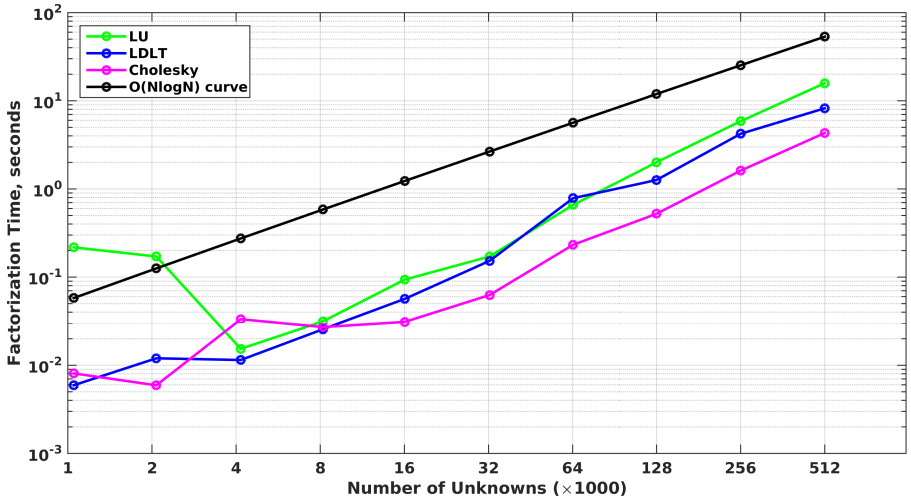

Figure 3.7: Processing time required for the factorization of the Gram matrices by using LU, LDLT, and Cholesky factorization techniques with respect to the number of unknowns.

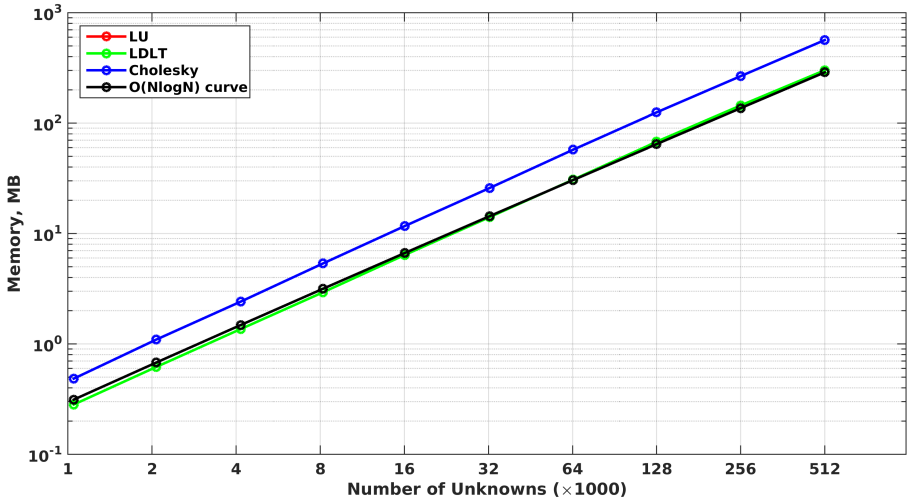

Figure 3.8: Required memory for the factorization of Gram matrices when using LU, LDLT, and Cholesky factorization techniques with respect to the number of unknowns.

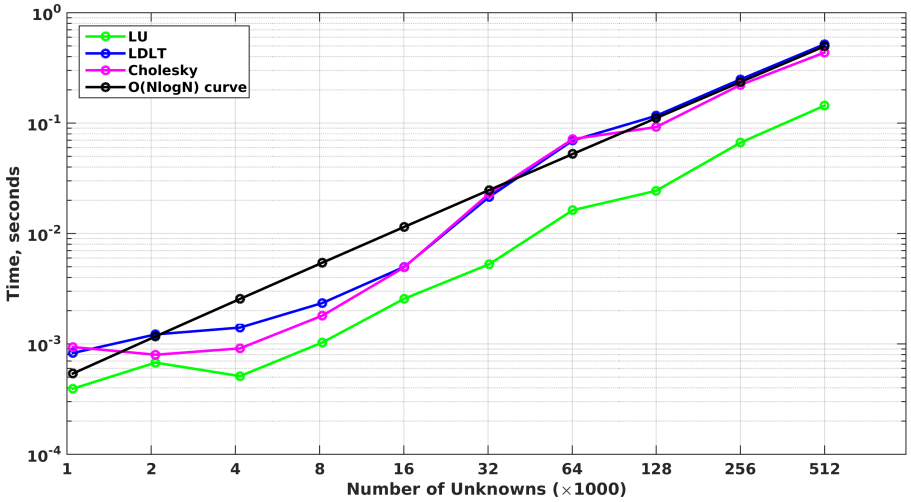

Figure 3.9: Mean inversion time when LU, LDLT, and Cholesky factorization techniques are used for the Gram matrices with respect to the number of unknowns.

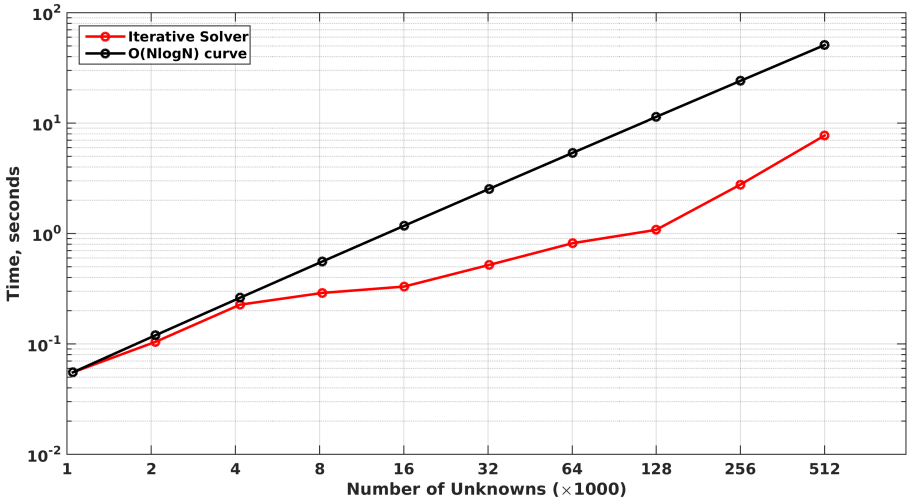

Figure 3.10: Mean inversion time when the iterative solver technique is used for the Gram matrices with respect to the number of unknowns.

of unknowns ranges from 1000 to 512,000 depending on the frequency. Comparisons of the factorization techniques are given in Figures 3.7, 3.8, and 3.9. Figure 3.7 shows the time to apply a factorization technique to the Gram matrices, Figure 3.8 shows the required memory to hold all matrices for the factorization, and Figure 3.9 shows the mean time for a multiplication with the inverse Gram matrix using the selected factorization technique. In addition, the mean time for an inversion by the iterative method is given in Figure 3.10. In these figures, mean time values are obtained by computing the mean of the processing times for 100 operations (multiplication or inversion). These figures show that the inversion of a Gram matrix can be obtained by using factorization techniques with $O(N \log N)$ complexity. However, application of a factorization technique requires huge memory, which easily reaches gigabytes for problems involving more than one million unknowns. Hence, using a factorization method, inversion of Gram matrices become a bottleneck when the mixed CFIE is employed for large-scale simulations [27]. On the other hand, handling the inversion of Gram matrices iteratively does not bring any additional memory requirement, making this strategy suitable when the problem size is large. We note that Gram matrices are extremely well-conditioned and their iterative solutions can be performed in few iterations.

3.4 Concluding Remarks

Since the inaccuracy of MFIE contaminates CFIE, the same mixed discretization scheme can be used to improve the accuracy of CFIE. On the other hand, when extending the use of rot-BC functions to CFIE, i.e., using rot-BC functions for testing MFIE and using RWG functions for testing EFIE, a direct convex combination does not eliminate internal resonances. To solve this problem, projection of testing spaces onto each other is required, which can be achieved via Gram matrices involving the inner products of RWG and rot-BC functions.

The optimal CFIE factor naturally depends on the discretization scheme. Therefore, the optimal CFIE factor in the context of its mixed discretization is investigated. In the case of the analysis of a sphere, 0.35 can be selected for the best convergence rate and accuracy for the mixed CFIE, whereas 0.2 was proposed for the classical

Galerkin discretization of CFIE. It is also observed that α values around 0.1 provides solutions with very small errors, which need further investigation.

While using MLFMA as an accelerator for the matrix-vector multiplications in the analysis of electrically large problems, inversion of Gram matrices should be handled carefully. This is investigated considering different factorization techniques and iterative solutions in the context of efficiency. The results show that an iterative technique should be preferred to avoid extra memory requirements that become bottlenecks when the factorization methods are used as the problem size grows.

CHAPTER 4

MAGNETIC-FIELD INTEGRAL EQUATION WITH DOUBLE LAYER MODELING

In this chapter, the internal resonance problem of MFIE is discussed in detail. Instead of using a CFIE implementation, a novel formulation that is only based on MFIE with double-layer modeling is proposed to mitigate internal resonances. Discretization of the proposed formulation is further discussed considering that it is purely based on MFIE. Also, in the context of the double-layer modeling, selection of inner layers, post-processing, and parameters, such as gap size between layers, are discussed in detail.

4.1 Internal Resonance Problem

Theoretically, electromagnetic fields do not penetrate into PEC objects. However, if such an object is analyzed with EFIE or MFIE, non-zero inner fields can be observed at some resonance frequencies. This phenomenon is known as the internal resonance problem. From the perspective of numerical solutions via the method of moments, we can consider a matrix equation as a result of the discretization. This matrix equation for EFIE or MFIE, in the most general form, can be written as

$$\bar{\boldsymbol{Z}} \cdot \boldsymbol{a} = \boldsymbol{w}. \tag{4.1}$$

Ideally, a unique solution of the equation given above is

$$\boldsymbol{a} = \bar{\boldsymbol{Z}}^{-1} \cdot \boldsymbol{w}. \tag{4.2}$$

However, using EFIE or MFIE, the matrix equation in (4.1) also satisfies

$$\bar{\boldsymbol{Z}} \cdot \boldsymbol{a}^{\mathrm{IRP}} = 0 \tag{4.3}$$

at a resonance frequency, where $\boldsymbol{a}^{\text{IRP}}$ is a non-zero solution that contaminates the solution. Therefore, (4.1) can be rewritten as

$$\bar{\boldsymbol{Z}} \cdot (\boldsymbol{a} + \boldsymbol{a}^{\text{IRP}}) = \boldsymbol{w} \tag{4.4}$$

at resonance frequencies. If the considered electromagnetic problem is formulated via EFIE, the internal resonance problem leads to increased numbers of iterations. However, resonance currents of EFIE do not radiate to far zone; thus EFIE can be used for the analysis of scattering problems that require correct far-zone field distributions, provided that ill-conditioning does not ruin the accuracy of solutions. In the case of MFIE, however, both near-zone and far-zone field distributions are inaccurate. All these resonances, which are characteristic properties of the geometry under investigation, become more significant as the size of the object becomes electrically large. In addition, although resonances are theoretically at discrete frequencies, destructive effects are observed to spread around resonance frequencies due to discretizations. Hence, MFIE is mostly impractical for electrically large problems.

As an example to demonstrate the internal resonance problem, a sphere centered at the origin with a radius of 300 mm is considered. The problem is analyzed via MFIE discretized with RWG functions on 20 mm triangles for a frequency range from 0.5 GHz to 1.5 GHz with 10 MHz steps. Electric and magnetic field intensity distributions are sampled on a plane, which divides the sphere into two equal pieces, as shown in Figure 4.1 and Figure 4.2, respectively. In both Figure 4.1 and Figure 4.2, resonant frequencies can easily be recognized since the inner fields are not zero as they should be for a PEC object. Spread of resonance effects at around resonance frequencies can also be observed in these results.

As another example, a sphere with a radius of 250 mm is considered and analyzed via MFIE (again discretized with RWG functions) on 20 mm triangles in the same frequency range. Electric and magnetic field intensity distributions in the near-zone region are computed and shown in Figure 4.3 and Figure 4.4, respectively. When electric and magnetic field intensity distributions of spheres with different sizes are compared, it can be observed that resonance frequencies shift (depending on the electrical size of the object), while the field patterns not only depend on the electrical size but also the discretization itself.

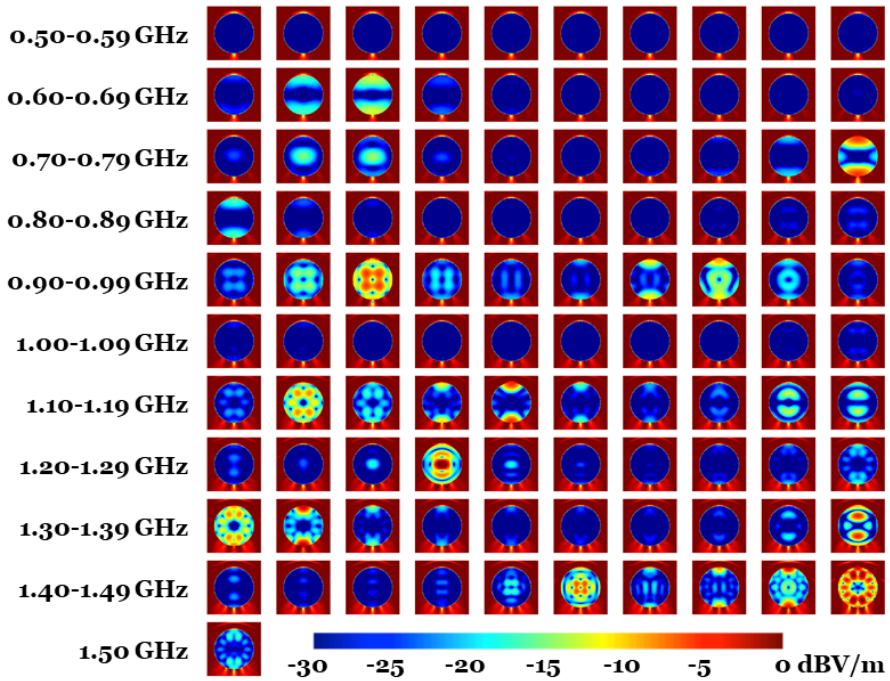

Figure 4.1: Near-zone electric field intensity at around a PEC sphere with 300 mm radius, which is excited by plane waves at different frequencies. The results are obtained by using MFIE.

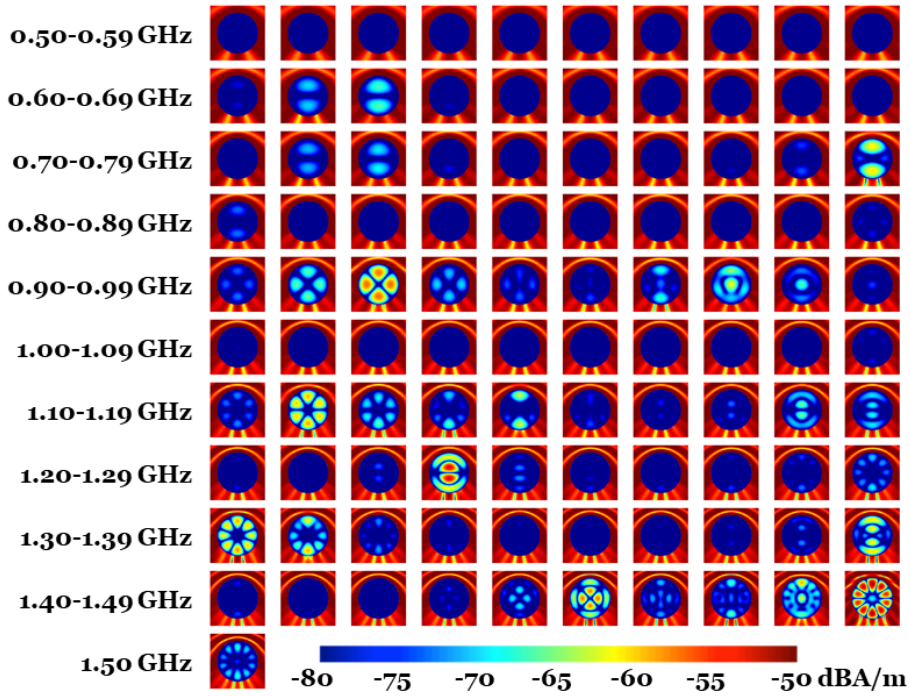

Figure 4.2: Near-zone magnetic field intensity at around a PEC sphere with 300 mm radius, which is excited by plane waves at different frequencies. The results are obtained by using MFIE.

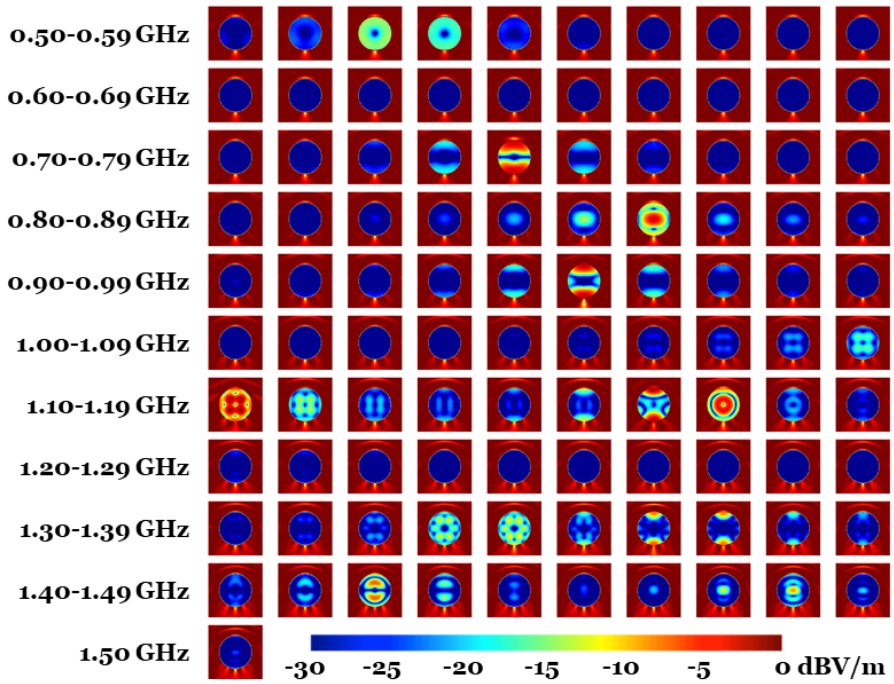

Figure 4.3: Near-zone electric field intensity at around a PEC sphere with 250 mm radius, which is excited by plane waves at different frequencies. The results are obtained by using MFIE.

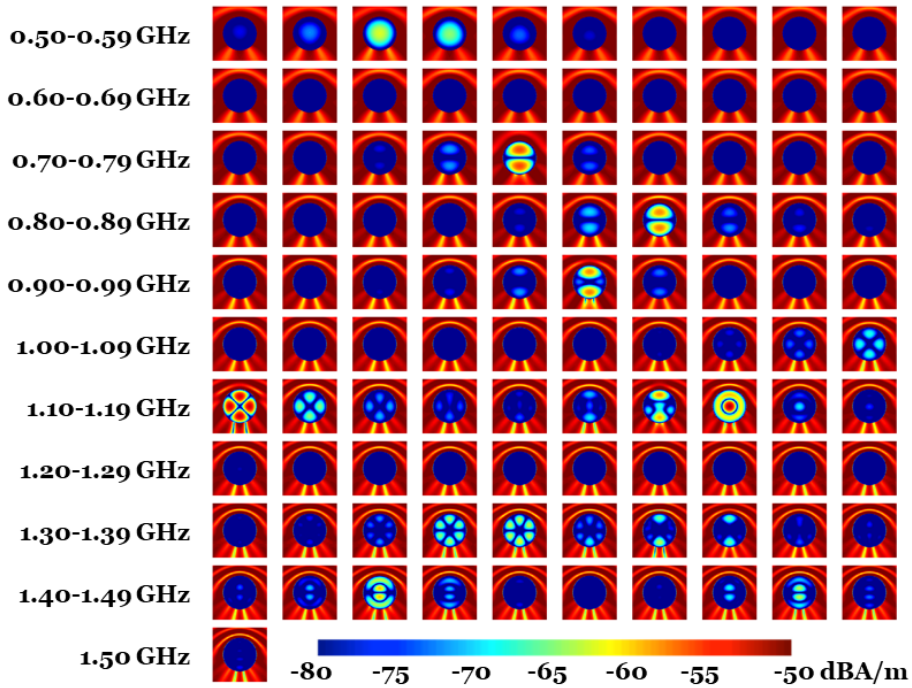

Figure 4.4: Near-zone magnetic field intensity at around a PEC sphere with 250 mm radius, which is excited by plane waves at different frequencies. The results are obtained by using MFIE.

4.2 MFIE with Double-Layer Modeling

One well-known method to overcome the internal resonance problem in the literature is to use CFIE, which is a linear combination of EFIE and MFIE. However, CFIE inherits the drawbacks of EFIE and MFIE. As discussed in Chapters 2 and 3, MFIE has inaccuracy issues, while EFIE is often ill-conditioned and its solutions require large numbers of iterations. Considering that the accuracy of MFIE can be improved via mixed discretization schemes, it becomes attractive to develop a formulation based on only MFIE that can provide high iterative convergence rates and easy hybridization with asymptotic techniques. In this thesis, we propose a novel MFIE formulation based on a double-layer modeling, which is free of internal resonances without using EFIE [28, 29].

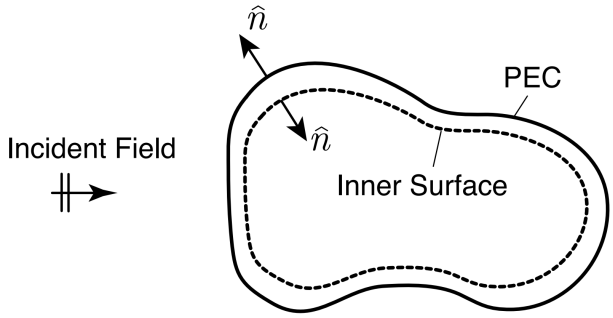

Figure 4.5: A double-layer modeling of the proposed formulation in order to eliminate internal resonances in MFIE.

In order to explain the idea behind the proposed formulation, we may consider a PEC object placed in free space as given in Figure 4.5. A hypothetical surface (named as "Inner Surface" in the figure) is placed inside the original surface of the object in order to mitigate internal resonances. The electric current density is expanded on both surfaces by using the RWG functions as basis functions. Boundary conditions are also applied on the inner surface to enforce the hypothetical currents to zero. When the actual surface is enumerated as the first surface and the hypothetical surface is enumerated as the second surface, the matrix equation, which defines the interactions of the discretization functions, can be written as

$$\begin{bmatrix} \bar{\boldsymbol{Z}}_{11} & \bar{\boldsymbol{Z}}_{12} \\ \bar{\boldsymbol{Z}}_{21} & \bar{\boldsymbol{I}}/2 \end{bmatrix} \cdot \begin{bmatrix} \boldsymbol{a} \\ \boldsymbol{b} \end{bmatrix} = \begin{bmatrix} \boldsymbol{w}_1 \\ \boldsymbol{w}_2 \end{bmatrix} . \tag{4.5}$$

In this equation, matrix elements $\bar{\boldsymbol{Z}}_{kl}$ defines the relationships between the surfaces for $k = 1, 2$ and $l = 1, 2$. Specifically, $\bar{\boldsymbol{Z}}_{11}$ is the impedance matrix corresponding to MFIE for the original geometry, while $\bar{\boldsymbol{Z}}_{12}$ and $\bar{\boldsymbol{Z}}_{21}$ represent magnetic-field interactions between the actual and hypothetical surfaces. For $\bar{\boldsymbol{Z}}_{22}$, only Gram-matrix calculations are performed between the discretization elements of the hypothetical surface. The right-hand side vectors are obtained as in the conventional MFIE. The new formulation is named MFIE-DL. Although there have been studies that investigate the use of dual surfaces [30, 31] for integral equations, they propose simply increasing the number of testing points without defining and using control currents on hypothetical surfaces. Therefore, the double-layer modeling proposed in this work is a completely novel strategy to mitigate internal resonances in MFIE without resorting to CFIE.

In the double-layer modeling, the constructed matrix equation is satisfied only if the electric current density on the inner (hypothetical) surface is zero. This means that the inner tangential magnetic field intensity is enforced to zero. As a result, the unique solution of (4.5) occurs as $\boldsymbol{a} = \bar{\boldsymbol{Z}}_{11}^{-1} \cdot \boldsymbol{w}_1$ and $\boldsymbol{b} = 0$, provided that the inner surface and its location are selected carefully.

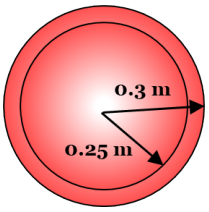

Figure 4.6: Double-layer modeling of a sphere (300 mm radius) using an inner hypothetical surface (sphere with 250 mm radius).

In order to demonstrate the proposed approach, analysis of a PEC sphere with 300 mm radius is considered, while another sphere with 250 mm radius is placed inside as the hypothetical surface for the double-layer modeling as shown in Figure 4.6. RWG functions are used as both testing and basis functions. Analysis of the double-layer

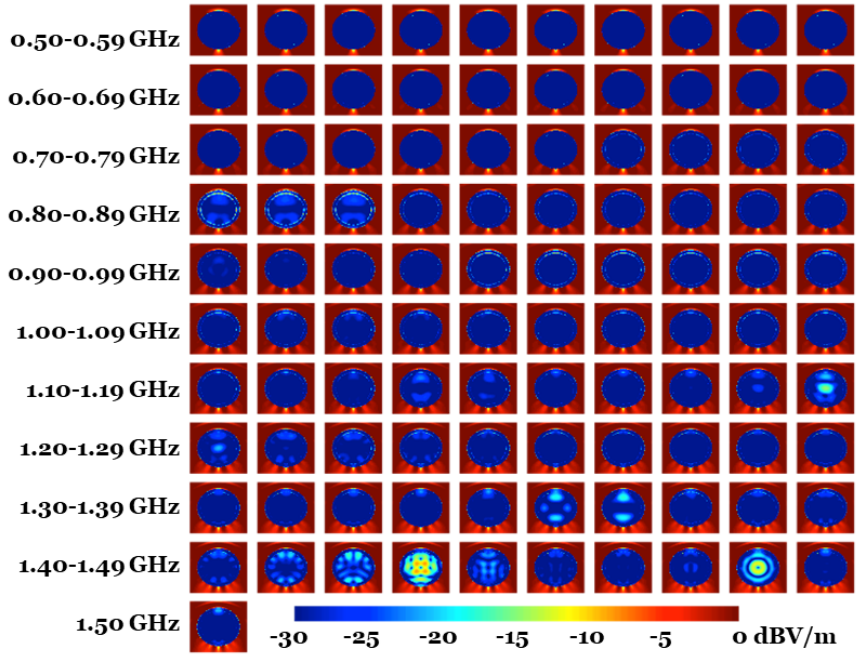

Figure 4.7: Near-zone electric field intensity at around a PEC sphere with 300 mm radius, which is excited by plane waves at different frequencies. The results are obtained by using MFIE-DL, which employs a sphere with 250 mm radius as the hypothetical inner surface.

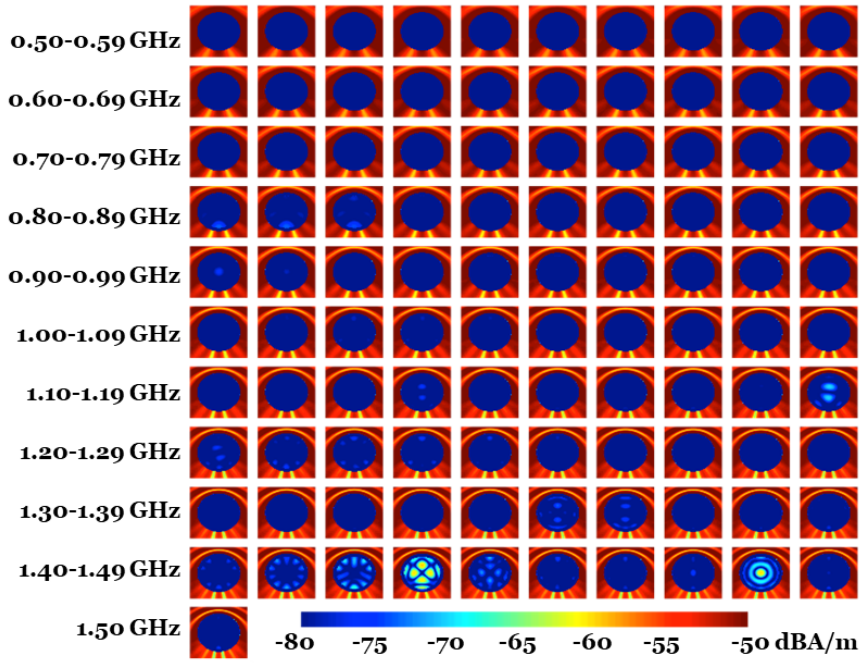

Figure 4.8: Near-zone magnetic field intensity at around a PEC sphere with 300 mm radius, which is excited by plane waves at different frequencies. The results are obtained by using MFIE-DL, which employs a sphere with 250 mm radius as the hypothetical inner surface.

model is performed in a frequency range from 0.5 GHz to 1.5 GHz with a step size of 10 MHz. The entire model is discretized with 20 mm triangles, which results in 6196 triangles on the outer surface and 4298 triangles on the inner surface. The near-zone electric and magnetic field intensity distributions are given in Figures 4.7 and 4.8, respectively. In these figures, it can be observed that resonance fields are mostly suppressed, leading to vanishingly small values inside the sphere. However, there are still remaining inner fields at some frequencies, e.g., at 0.81 GHz. In addition, new nonzero field distributions, which are not visible in the direct analyses of spheres with 300 mm and 250 mm radii, are observed at 1.43 and 1.48 GHz. These results show that, while the double-layer modeling operates as desired, it should be investigated further to reach an implementation that is completely free of internal resonances.

4.3 Accurate Testing of MFIE-DL

MFIE-DL is purely based on MFIE formulation, thus it holds all the numerical drawbacks of MFIE. Testing of MFIE-DL should be handled carefully, not only because of $\bar{\boldsymbol{Z}}_{11}$, but also due to $\bar{\boldsymbol{Z}}_{22}$ that is purely the Gram matrix. As shown in Chapter 2, when the currents are expanded in terms of RWG functions, testing should be performed with rot-BC functions for accurate results with MFIE. Based on this finding, the mixed discretization scheme is also applied to MFIE-DL.

The near-zone electric and magnetic field intensity distributions obtained by using MFIE-DL with rot-BC testing functions are shown in Figure 4.9 and Figure 4.10, respectively. Similar to the previous set shown in Figures 4.7 and 4.8, we consider again a PEC sphere with 300 mm radius together with a hypothetical surface in the shape of a sphere of radius 250 mm. In these figures, it is observed that better suppression of inner fields is obtained by using rot-BC testing functions instead of RWG testing functions. However, there are still remarkable inner fields at 1.19 GHz, 1.43 GHz, and 1.48 GHz. These remaining internal fields are due to the fact that rot-BC testing functions improve the overall accuracy and make resonances sharper, while they do not eliminate the internal resonance problem.

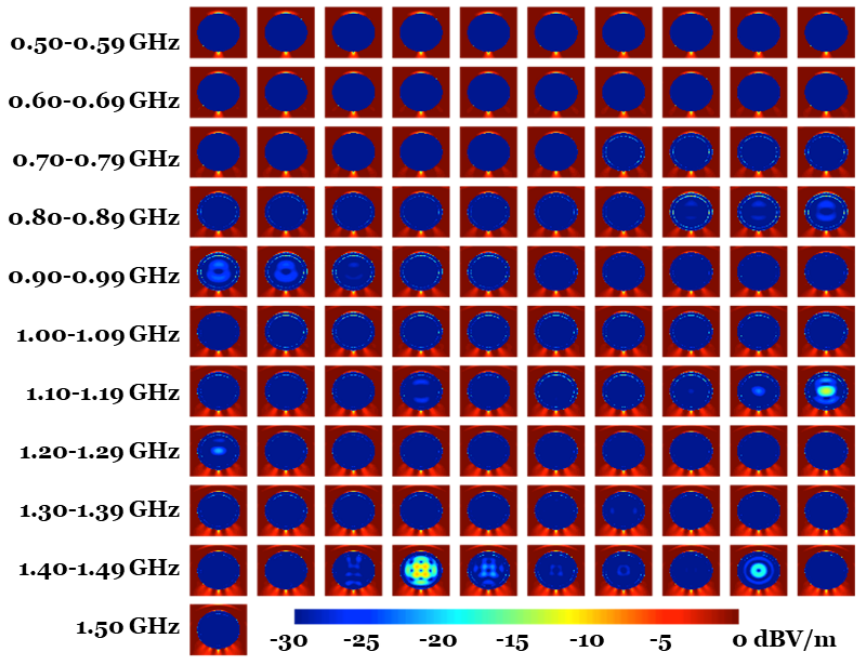

Figure 4.9: Near-zone electric field intensity at around a PEC sphere with 300 mm radius, which is excited by plane waves at different frequencies. The results are obtained by using mixed-discretized MFIE-DL, which employs a sphere with 250 mm radius as the hypothetical inner surface.

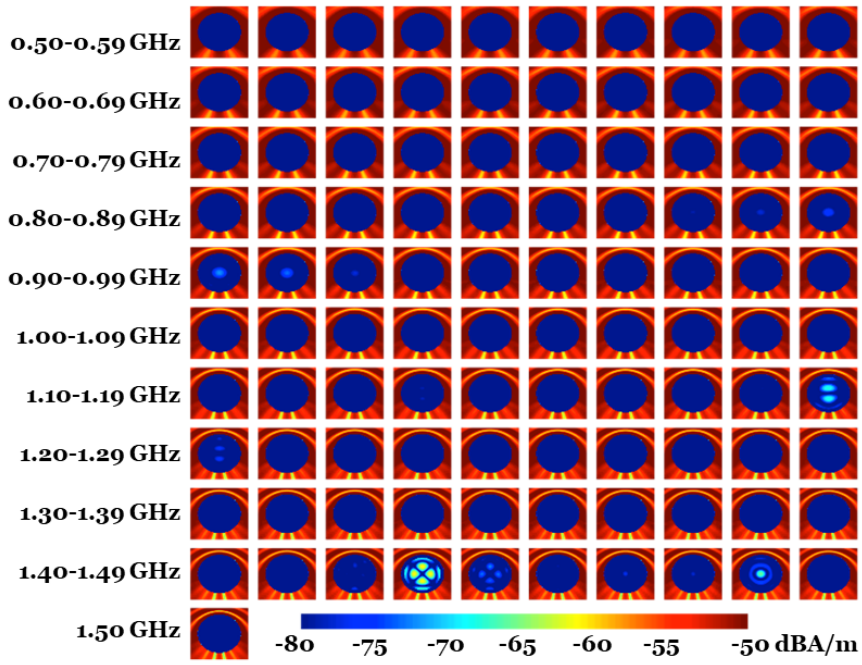

Figure 4.10: Near-zone magnetic field intensity at around a PEC sphere with 300 mm radius, which is excited by plane waves at different frequencies. The results are obtained by using mixed-discretized MFIE-DL, which employs a sphere with 250 mm radius as the hypothetical inner surface.

4.4 Selective Radiation

Until now, in double-layer modeling, the electric and magnetic field intensity distributions are computed by using the current distributions on both (actual and hypothetical) surfaces. However, for a given double-layer model, the expected solution of MFIE-DL is $\boldsymbol{a} = \bar{\boldsymbol{Z}}_{11}^{-1} \cdot \boldsymbol{w}_1$ and $\boldsymbol{b} = 0$, which states that the expansion coefficients of the inner surface must be zero. In order to verify this for the problem discussed so far, norms of current coefficients of each surface are plotted with respect to frequency in Figure 4.11. In this figure, it is observed that outer coefficients are consistent, while inner coefficients depend on the used testing functions. Also, it is observed that testing with rot-BC functions provides smaller inner coefficient values, verifying the better accuracy provided by correct testing. It is also remarkable that when we compare this figure with the corresponding near-zone field distributions, it is observed that the problematic frequencies, at which remaining inner fields exist, correspond to those with increased inner coefficients for both RWG and rot-BC testing functions. Considering that inner currents should ideally be zero, a post-processing is proposed

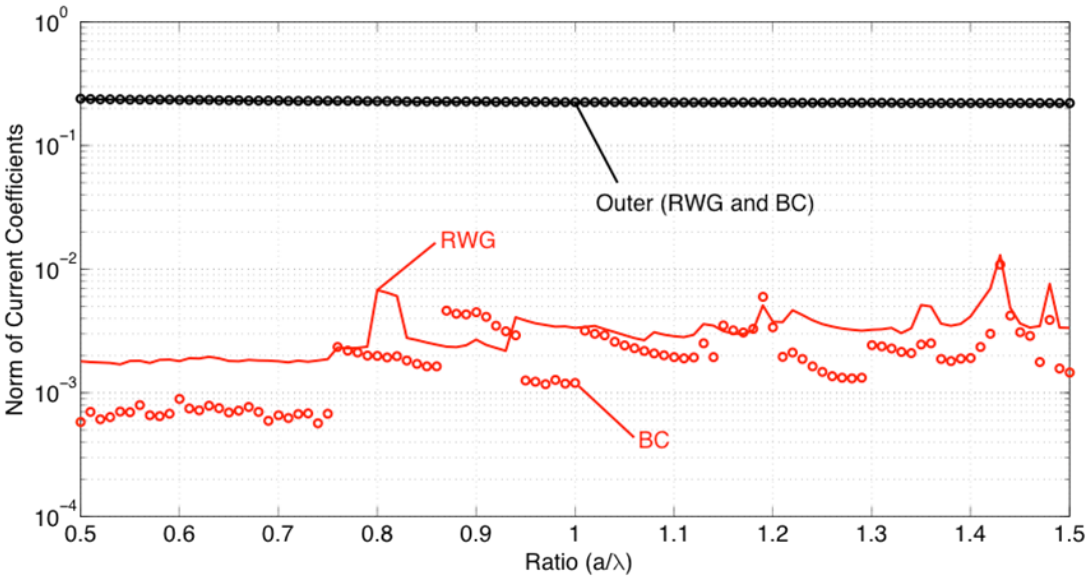

Figure 4.11: Norm of current coefficients in the solutions of a PEC sphere with 300 mm radius. The results are obtained by using MFIE-DL, which uses a sphere with 250 mm radius as the hypothetical surface. The plots are obtained when RWG and rot-BC functions are used as testing functions.

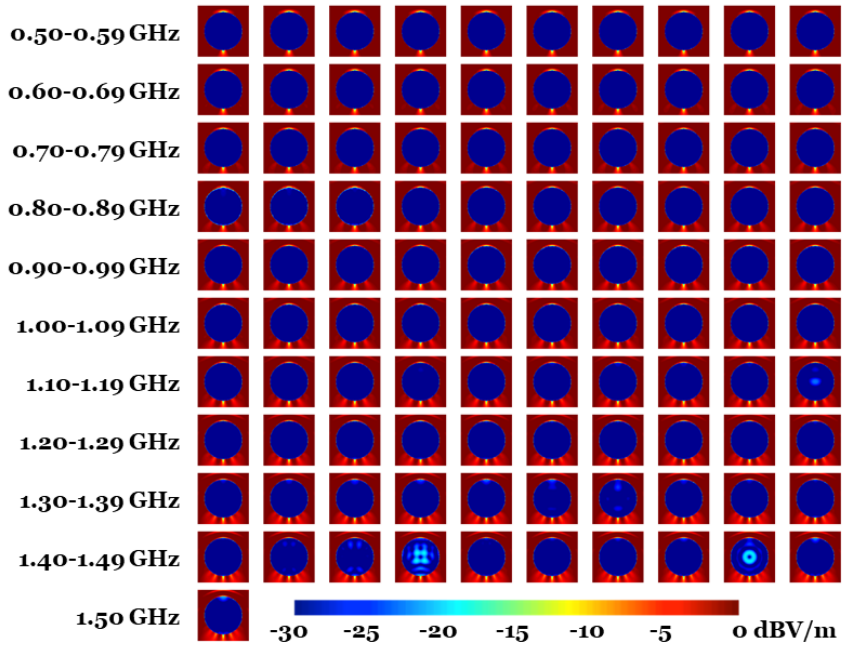

Figure 4.12: Near-zone electric field intensity at around a PEC sphere with 300 mm radius, which is excited by plane waves at different frequencies. The results are obtained via selective radiation in MFIE-DL, which employs a sphere with 250 mm radius as the hypothetical inner surface.

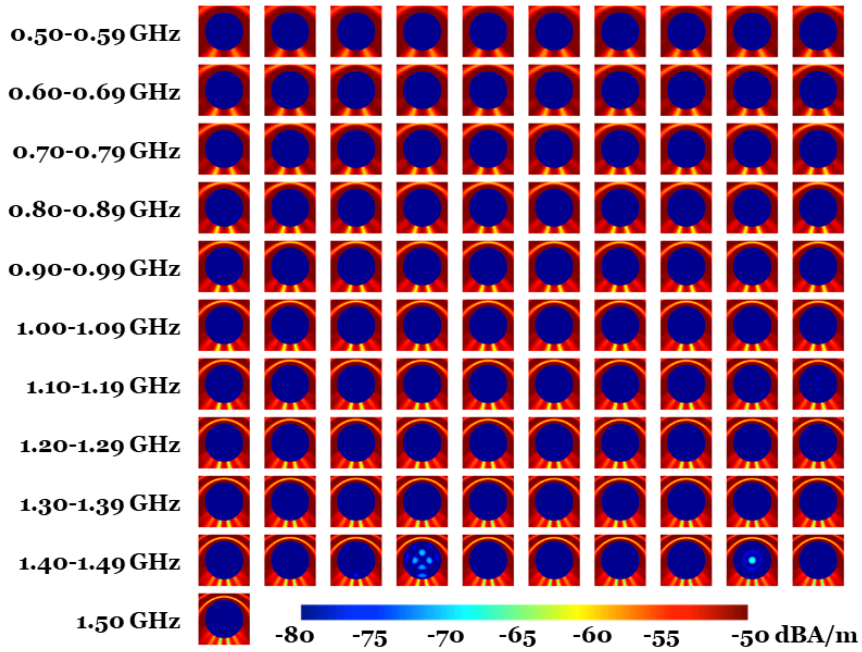

Figure 4.13: Near-zone magnetic field intensity at around a PEC sphere with 300 mm radius, which is excited by plane waves at different frequencies. The results are obtained via selective radiation in MFIE-DL, which employs a sphere with 250 mm radius as the hypothetical inner surface.

to select the current coefficients only on the actual surfaces to radiate. Specifically, the near-zone electric and magnetic field intensity values are computed with the radiation of only outer surface currents and this process is named "selective radiation". For the sphere problem discussed so far, the near-zone electric and magnetic field intensity distributions are given for the case of testing with RWG functions in Figures 4.12 and 4.13. In these figures, it is observed that inner fields are significantly suppressed at all frequencies, except some minor fields at 1.19 GHz, 1.43 GHz, and 1.48 GHz, even with RWG testing functions. Hence, selective radiation is an essential operation for MFIE-DL to obtain accurate results. But, as shown below, further improvements are possible by carefully selecting inner surfaces, particularly via adaptive gaps.

4.5 On the Selection of Inner Layers

As shown above, most of the internal resonances can be eliminated by using MFIE-DL and applying selective radiation. Also, it has been shown that the accuracy of MFIE-DL can be improved significantly by using rot-BC testing functions. On the other hand, there can be remaining resonance frequencies, depending on the selection of inner surfaces. For example, using an inner sphere of radius 250 mm for a PEC sphere of radius 300 mm is a suitable choice found after many trials. In order to demonstrate the importance of the selection of the inner surface, two more cases are investigated for the same scattering problem. The first model (Figure 4.14a) is obtained by creating a triple layer model with the addition of another inner sphere of

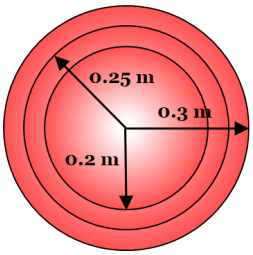

(a) Triple-layer modeling of a sphere with two inner spheres of radii 0.25 m and 0.2 m.

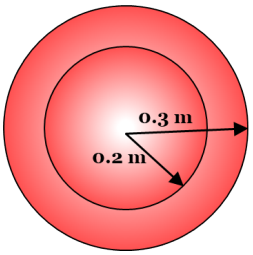

(b) Double-layer modeling of a sphere with an inner sphere of radius 0.2 m.

Figure 4.14: Alternative models for multilayer modeling.

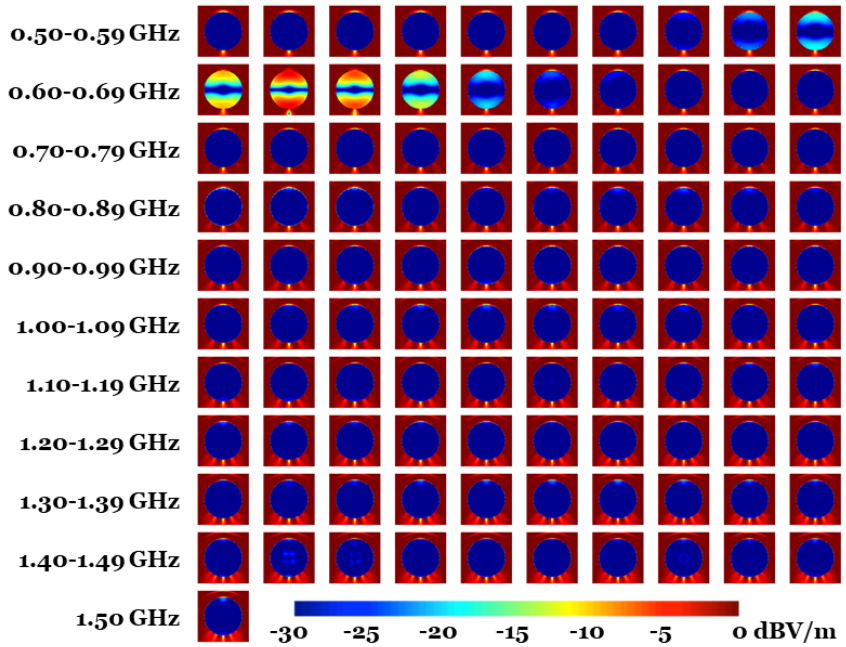

Figure 4.15: Near-zone electric field intensity at around a PEC sphere with 300 mm radius, which is excited by plane waves at different frequencies. The results are obtained via selective radiation in a triple-layer modeling.

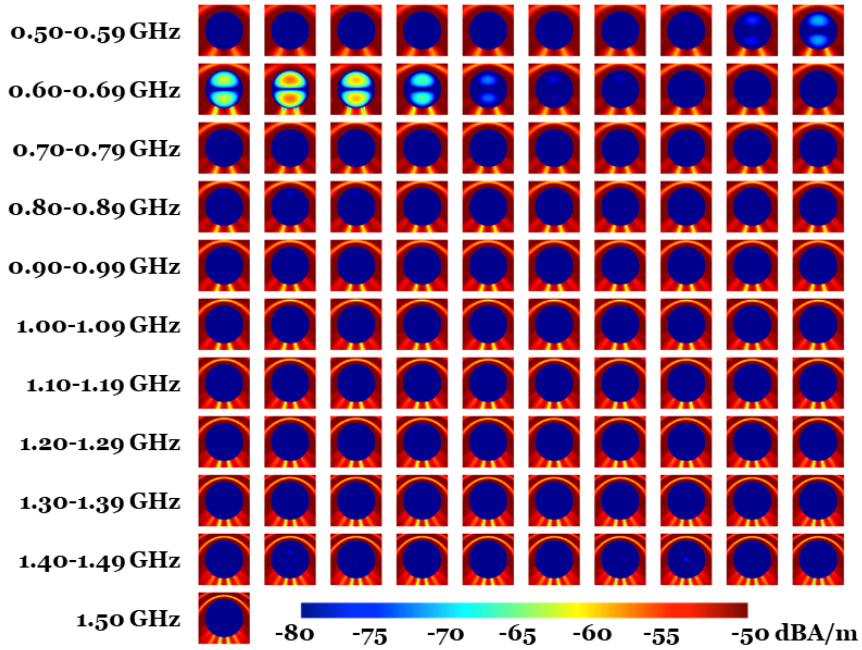

Figure 4.16: Near-zone magnetic field intensity at around a PEC sphere with 300 mm radius, which is excited by plane waves at different frequencies. The results are obtained via selective radiation in a triple-layer modeling.

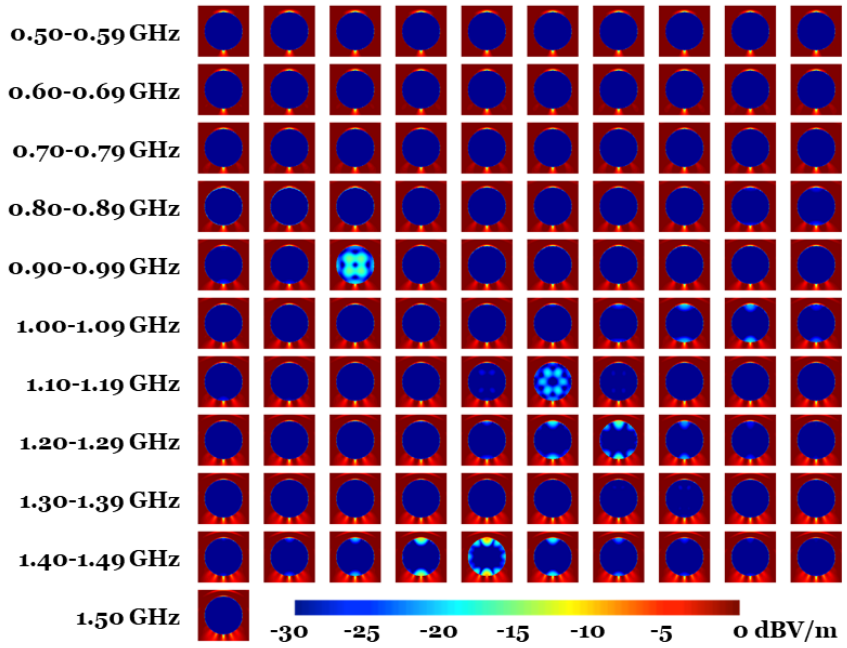

Figure 4.17: Near-zone electric field intensity at around a PEC sphere with 300 mm radius, which is excited by plane waves at different frequencies. The results are obtained via selective radiation in MFIE-DL, which employs a sphere with 200 mm radius as the hypothetical inner surface.

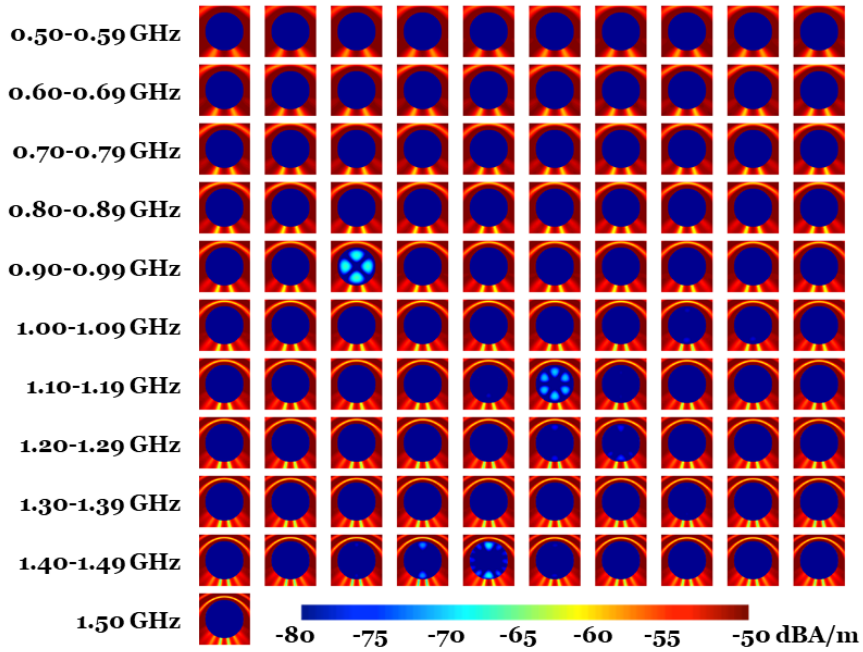

Figure 4.18: Near-zone magnetic field intensity at around a PEC sphere with 300 mm radius, which is excited by plane waves at different frequencies. The results are obtained via selective radiation in MFIE-DL, which employs a sphere with 200 mm radius as the hypothetical inner surface.

radius 200 mm to the existing double-layer model. The second model (Figure 4.14b) is obtained by decreasing the radius of the inner sphere to 200 mm. Both models are discretized with 20 mm triangles, leading to $13,292$ triangles for the triple-layer model and $10,494$ triangles for the double-layer model (with smaller inner sphere). Simulations are carried out in the same frequency range from 0.5 GHz to 1.5 GHz with a step size of 10 MHz. Near-zone field intensity distributions are computed with the selective radiation as described above. The electric and magnetic field intensity distributions for the triple-layer model are given in Figures 4.15 and 4.16, respectively. In these figures, it can be observed that the triple-layer model mitigates the resonances of MFIE-DL at higher frequencies, while it leads to new issues at lower frequencies, e.g., at 0.6 GHz. Therefore, increasing the number of layers does not provide better results. The electric and magnetic field intensity distributions for the double layer modeling using a smaller inner sphere of radius 200 mm are given in Figures 4.17 and 4.18, respectively. In these figures, it is observed that MFIE-DL mitigates the internal resonances at many frequencies, while there are frequencies, at which nonzero inner fields exist. These problematic frequencies are different from those when using MFIE-DL with the inner surface of radius 250 mm. For example at 0.92 GHz, powerful inner fields, which do not exist in the earlier set, can be observed. This new resonance seems to be introduced due to the increasing gap between the outer and inner layers.

4.6 Adaptive Gap

Investigation of alternative scenarios, some of which are shown above, leads to two important results. First, the distance between the actual and hypothetical surfaces should not be too large to avoid internal fields between them. Second, depending on the distance between the surfaces, some inner fields may still occur at certain frequencies. These remaining issues can be mitigated by using adaptive gaps that change with respect to frequency. Based on the experience on the earlier simulations, a $\lambda/10$ adaptive gap is investigated to obtain a better performance with MFIE-DL. When this kind of a gap selection is applied, the distance between the surfaces changes with respect to frequency so that inner fields can effectively be suppressed.

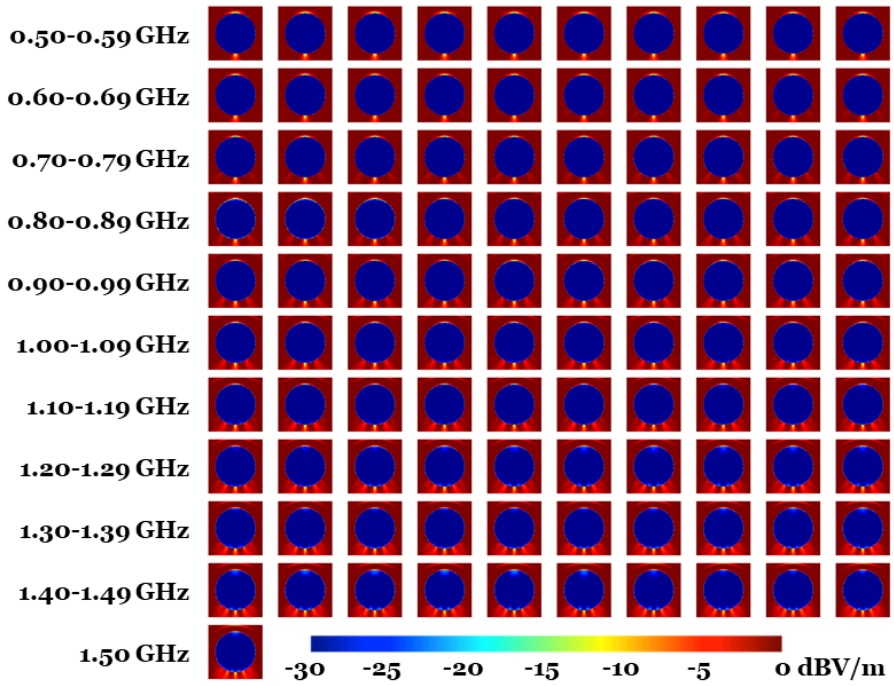

Figure 4.19: Near-zone electric field intensity at around a PEC sphere with 300 mm radius, which is excited by plane waves at different frequencies. The results are obtained via selective radiation in MFIE-DL with an adaptive gap between surfaces.

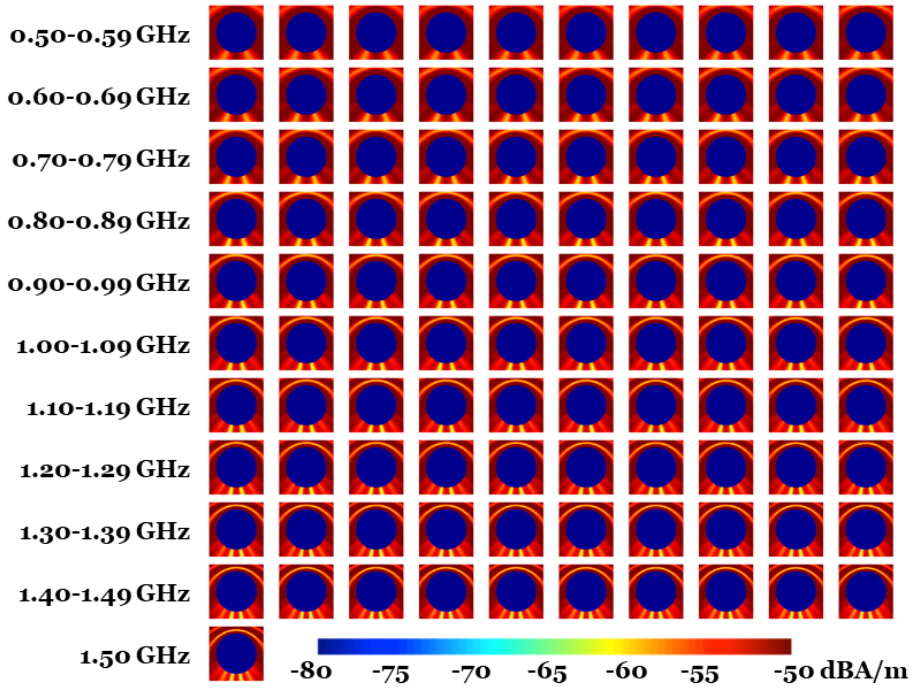

Figure 4.20: Near-zone magnetic field intensity at around a PEC sphere with 300 mm radius, which is excited by plane waves at different frequencies. The results are obtained via selective radiation in MFIE-DL with an adaptive gap between surfaces.

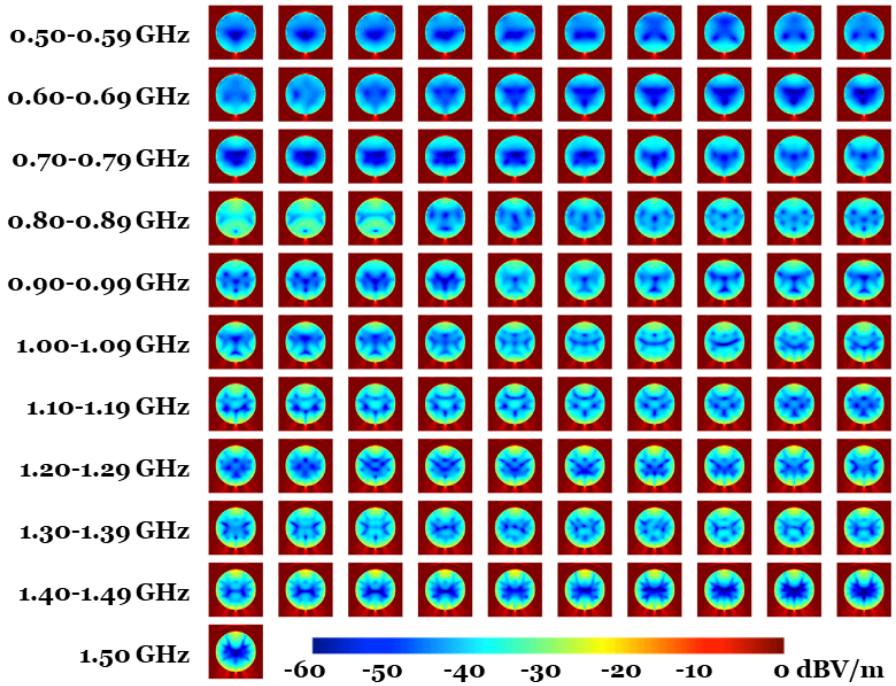

Figure 4.21: Repetition of the results in Figure 4.19 with the change of color range to observe very small internal fields.

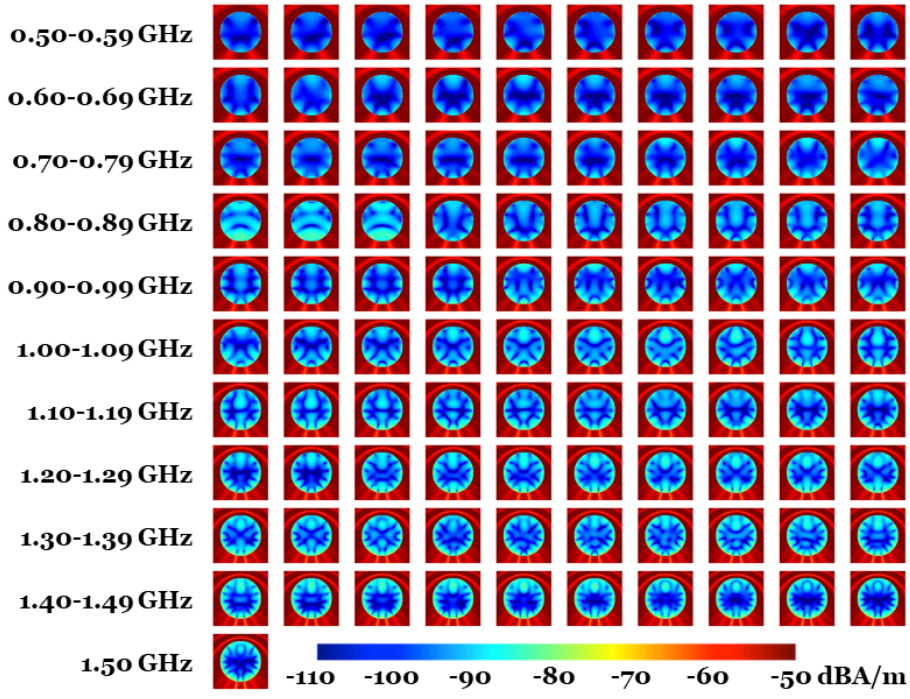

Figure 4.22: Repetition of the results in Figure 4.20 with the change of color range to observe very small internal fields.

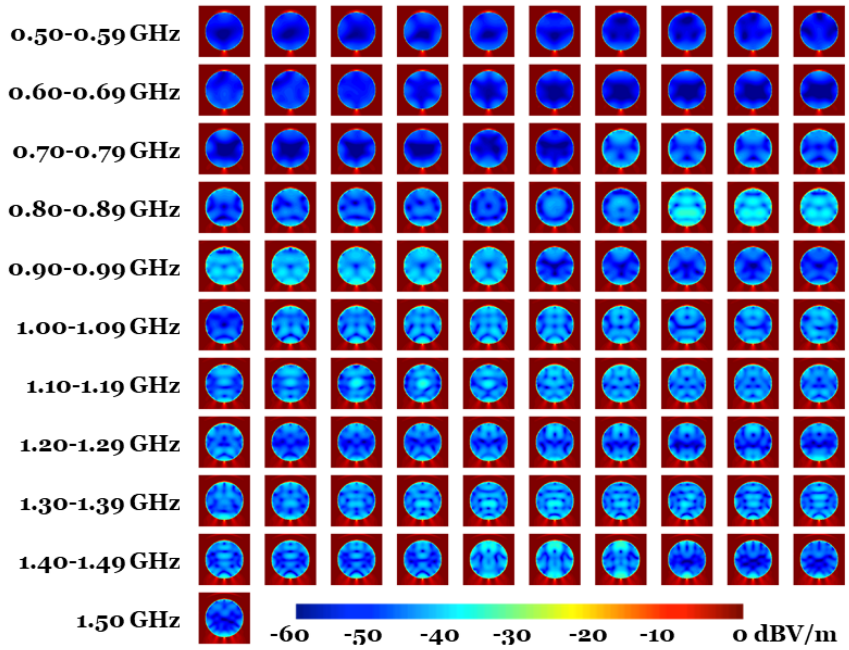

Figure 4.23: Near-zone electric field intensity at around a PEC sphere with 300 mm, which is excited by plane waves at different frequencies. The results are obtained via selective radiation in MFIE-DL with an adaptive gap between surfaces and by employing rot-BC functions for testing.

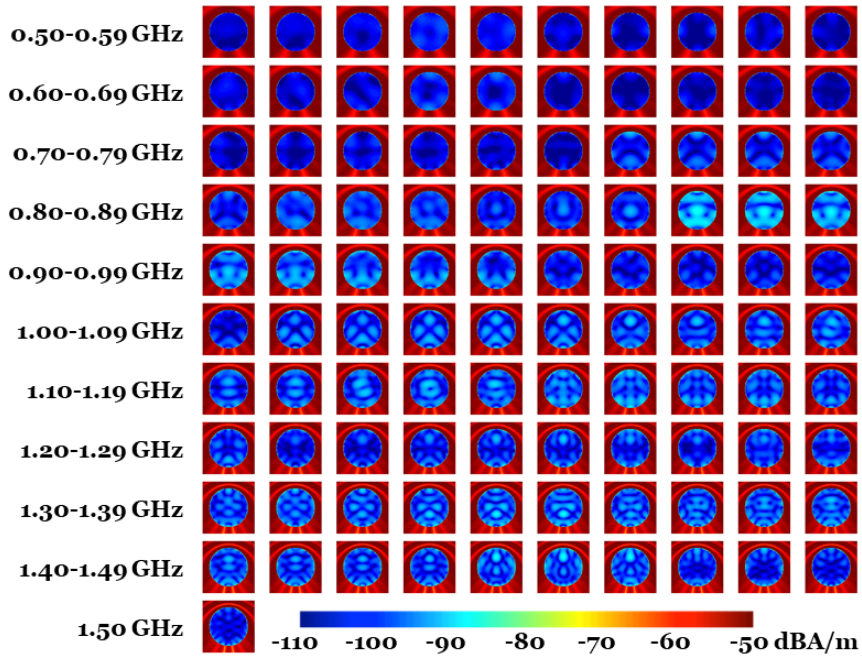

Figure 4.24: Near-zone magnetic field intensity at around a PEC sphere with 300 mm, which is excited by plane waves at different frequencies. The results are obtained via selective radiation in MFIE-DL with an adaptive gap between surfaces and by employing rot-BC functions for testing.

In order to investigate the effect of the $\lambda/10$ adaptive gap, double-layer models of the PEC sphere with 300 mm radius are considered. In this case, the radius of the inner sphere at a frequency f can be written as

$$r_{\text{inner}} = 0.3 - \lambda/10, \tag{4.6}$$

where λ is the wavelength corresponding to the frequency f. MFIE-DL with adaptive gap is investigated in the same frequency range, while selective radiation is applied to obtain field distributions in the near zone. Galerkin scheme with RWG functions is used for the discretization. The electric and magnetic field intensity distributions are given in Figures 4.19 and 4.20, respectively. In these figures, it is easily noticed that all resonances are successfully mitigated. In order to observe very weak inner fields, the color ranges of the plots in Figures 4.19 and 4.20 are changed from 30 dB to 60 dB, leading to the plots 4.21 and 4.22, respectively. While the results are already successful, testing with rot-BC functions is further applied to MFIE-DL with selective radiation and adaptive gap for the same set of problems. The electric and magnetic field intensity distributions for this case are shown with a color range of 60 dB in Figures 4.23 and 4.24, respectively. In these figures, it can be observed that a superior inner-field suppression is obtained.

4.7 Analysis of Numerical Results

The inner fields related to the internal resonance problem are successfully suppressed by using MFIE-DL with adaptive gap and selective radiation. The suppression of inner fields are discussed, considering near-zone field distributions until now. After the successful suppression of inner fields, it is expected to obtain accurate far-zone scattering computations with MFIE-DL. To verify this, the normalized backscattered RCS of the sphere with 0.3 m radius is shown in Figure 4.25. This sphere is analyzed with the classical discretizations of EFIE, MFIE, and CFIE in addition to MFIE-DL with the help of adaptive gap and selective radiation. In Figure 4.25, it can be observed that the results obtained with MFIE-DL follow Mie-series solutions and the internal resonances are successfully suppressed. In addition, accuracy of MFIE-DL can significantly be improved with the mixed discretization scheme. Figure 4.26 shows the corresponding numbers of GMRES iterations. It is observed that MFIE-DL

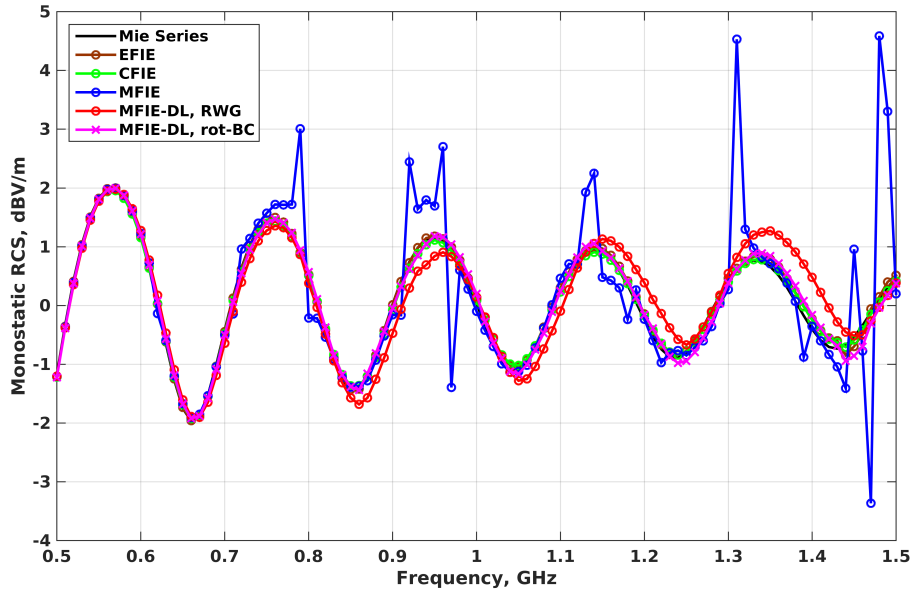

Figure 4.25: Normalized backscattered RCS with respect to the Mie-series solutions of a sphere with 0.3 m radius from 0.5 GHz to 1.5 GHz. The results are obtained with the classical discretizations of EFIE, CFIE, MFIE, and MFIE-DL, as well as with the mixed discretization of MFIE-DL.

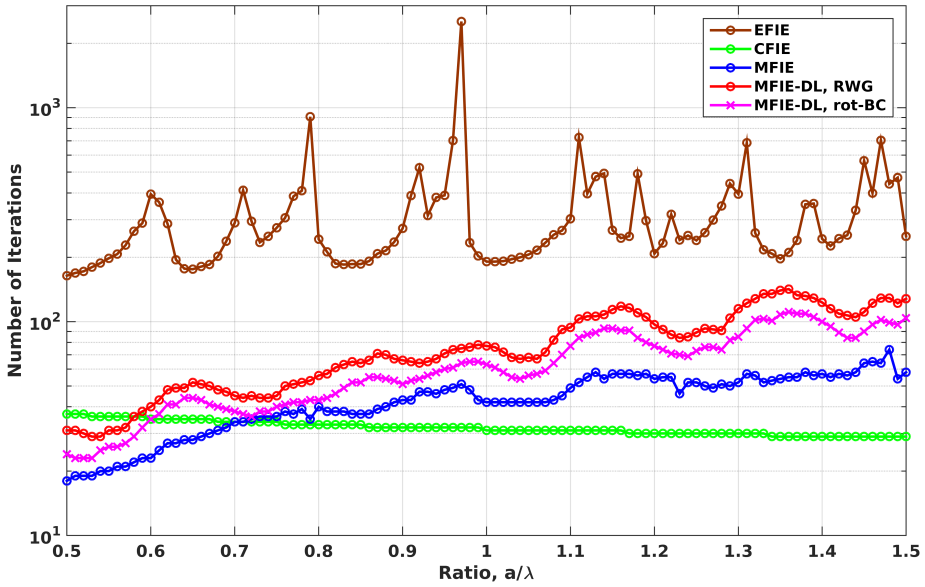

Figure 4.26: Numbers of iterations required for the analysis of a sphere with 0.3 m radius from 0.5 GHz to 1.5 GHz. The results are obtained with the classical discretizations of EFIE, CFIE, MFIE, and MFIE-DL, as well as with the mixed discretization of MFIE-DL.

implementations require smaller numbers of iterations than EFIE, whereas they have slower convergence rates in comparison to the conventional MFIE and CFIE. Spikes in the numbers of iterations for EFIE show the sensitivity of this formulation due to internal resonances. In the context of MFIE-DL, it can also be observed that iteration counts can be decreased at all frequencies by using the mixed discretization scheme.

4.8 Concluding Remarks

Due to the internal resonance problem, both near-zone and far-zone field intensity distributions obtained with MFIE are inaccurate, while the required numbers of iterations for solutions tend to increase at resonance frequencies. As an alternative to the well-known CFIE, which inherits the drawbacks of both EFIE and MFIE, a novel double-layer formulation that is purely based on MFIE is proposed and implemented. Using the developed implementation, suppression of inner fields due to internal resonances is clearly shown with numerical results.

Despite it is free of internal resonances, MFIE-DL still has accuracy issues encountered in MFIE. Therefore, testing with rot-BC functions is considered to obtain better accuracy with MFIE-DL. The unique solution of MFIE-DL is $\boldsymbol{a} = \bar{\boldsymbol{Z}}^{-1} \cdot \boldsymbol{w}_1$ and $\boldsymbol{b} = 0$, which states that expansion coefficients for the hypothetical inner surfaces must be zero. Since numerical solutions may lead residual currents on inner surfaces, more accurate results can be obtained with the radiation of only actual currents. It is shown via numerical examples that selective radiation should be an essential component of MFIE-DL to obtain accurate results.

Numerical results show that inner surfaces must be carefully selected for satisfactory suppression of internal fields in double-layer modeling. Considering that the distance between the surfaces strongly affects the suppression of fields, the use of adaptive gaps is proposed for better performances with MFIE-DL.

The final implementation of mixed-discretized MFIE-DL provides excellent results in terms of both accuracy and efficiency when it is used with adaptive gaps and selective radiation.

CHAPTER 5

CONCLUSIONS

In this work, MFIE for numerical solutions of electromagnetic problems involving three-dimensional PEC objects is studied in terms of accuracy and efficiency. Considering the state-of-the-art on this topic, a particular focus of this study is the selection of basis and testing functions in MFIE. It is shown that a mixed discretization scheme using RWG basis functions and rot-BC testing functions is very suitable for MFIE to obtain accurate results and well-conditioned matrix equations. Moreover, it is demonstrated that using three-point Gaussian quadrature rule to compute test integrals is essential for accuracy and fast iterative solutions.

Mixed discretization scheme of MFIE is extended to obtain better accuracy with CFIE. However, a direct convex combination of the classical Galerkin discretization of EFIE and the mixed discretization of MFIE does not eliminate internal resonances. Therefore, reflecting discretization spaces onto each other via Gram matrices is essential for the implementation of CFIE using mixed discretizations. The mixed discretization of CFIE is also investigated in the context of electrically large problems solved with MLFMA. The inversion of Gram matrices via iterative solvers is proposed considering computational complexity and memory requirements.

Finally, a novel double-layer formulation (MFIE-DL) is proposed as an alternative to mitigate the internal resonance problem without resorting to CFIE. Since the formulation is purely based on MFIE, the mixed discretization scheme is also proposed for MFIE-DL for better accuracy and iterative convergence rates. In the context of the double-layer modeling, selection of the hypothetical (inner) surface is discussed and the strategy of adaptive gap is proposed for the best results. Moreover, selective radiation of outer currents is proposed as the new formulation is based on suppressing

hypothetical inner currents. Numerical results shows that resonance-free results with high accuracy can be obtained with a mixed-discretized MFIE-DL when it is used together with the adaptive-gap strategy and selective radiation.

REFERENCES

[1] R. E. Hodges and Y. Rahmat-Samii, "The evaluation of MFIE integrals with the use of vector triangle basis functions," *Microwave and Optical Technology Letters*, vol. 14, no. 1, pp. 9–14, 1997.

[2] J. M. Rius, E. Ubeda, and J. Parron, "On the testing of the magnetic field integral equation with RWG basis functions in method of moments," *IEEE Transactions on Antennas and Propagation*, vol. 49, no. 11, pp. 1550–1553, Nov. 2001.

[3] Davis and Warnick, "High-order convergence with a low-order discretization of the 2-D MFIE," *IEEE Antennas and Wireless Propagation Letters*, vol. 3, pp. 355–358, 2004.

[4] Ö. Ergül and L. Gürel, "Investigation of the inaccuracy of the MFIE discretized with the RWG basis functions," in *IEEE Antennas and Propagation Society Symposium*, 2004, pp. 3393–3396.

[5] Ö. Ergül and L. Gürel, "Improving the accuracy of the MFIE with the choice of basis functions," in *IEEE Antennas and Propagation Society Symposium*, 2004, pp. 3389–3392.

[6] E. Ubeda and J. M. Rius, "Curl-conforming MFIE in the analysis of perfectly conducting sharply-edged objects," in *IEEE Antennas and Propagation Society Symposium*, 2004, pp. 4052–4055.

[7] Ö. Ergül and L. Gürel, "Solid-angle factor in the magnetic-field integral equation," *Microwave and Optical Technology Letters*, vol. 45, no. 5, pp. 452–456, 2005.

[8] L. Gürel and Ö. Ergül, "Singularity of the magnetic-field Integral equation and its extraction," *IEEE Antennas and Wireless Propagation Letters*, vol. 4, pp. 229–232, 2005.

[9] Ö. Ergül and L. Gürel, "Improved testing of the magnetic-Field integral equation," *IEEE Microwave and Wireless Components Letters*, vol. 15, no. 10, pp. 615–617, Oct. 2005.

[10] E. Ubeda and J. M. Rius, "MFIE MoM-formulation with curl-conforming basis functions and accurate kernel integration in the analysis of perfectly conducting sharp-edged objects," *Microwave and Optical Technology Letters*, vol. 44, no. 4, pp. 354–358, 2005.

[11] E. Ubeda and J. M. Rius, "Monopolar divergence-conforming and curl-conforming low-order basis functions for the electromagnetic scattering analysis," *Microwave and Optical Technology Letters*, vol. 46, no. 3, pp. 237–241, 2005.

[12] Ö. Ergül and L. Gürel, "The use of curl-conforming basis functions for the magnetic-field integral equation," *IEEE Transactions on Antennas and Propagation*, vol. 54, no. 7, pp. 1917–1926, Jul. 2006.

[13] Ö. Ergül and L. Gürel, "Improving the accuracy of the magnetic field integral equation with the linear-linear basis functions," *Radio Science*, vol. 41, no. 4, 2006.

[14] E. Ubeda and J. M. Rius, "Novel monopolar MFIE MoM-discretization for the scattering analysis of small objects," *IEEE Transactions on Antennas and Propagation*, vol. 54, no. 1, pp. 50–57, Jan. 2006.

[15] Ö. Ergül and L. Gürel, "Linear-linear basis functions for MLFMA solutions of magnetic-field and combined-field integral equations," *IEEE Transactions on Antennas and Propagation*, vol. 55, no. 4, pp. 1103–1110, Apr. 2007.

[16] S. Rao, D. Wilton, and A. Glisson, "Electromagnetic scattering by surfaces of arbitrary shape," *IEEE Transactions on Antennas and Propagation*, vol. 30, no. 3, pp. 409–418, May 1982.

[17] A. Buffa and S. H. Christiansen, "A dual finite element complex on the barycentric refinement," *Math. Comput.*, vol. 260, pp. 1743–1769, 2007.

[18] K. Cools, F. P. Andriulli, F. Olyslager, and E. Michielssen, "Improving the MFIE's accuracy by using a mixed discretization," in *2009 IEEE Antennas and Propagation Society International Symposium*, 2009.

[19] K. Cools, F. P. Andriulli, D. D. Zutter, and E. Michielssen, "Accurate and conforming mixed discretization of the MFIE," *IEEE Antennas and Wireless Propagation Letters*, vol. 10, pp. 528–531, 2011.

[20] S. Yan, J. Jin, and Z. Nie, "On the testing of the identity operator and the accuracy improvement of the second-kind SIEs," in *2011 IEEE International Symposium on Antennas and Propagation*, 2011, pp. 3185–3188.

[21] S. Yan, J. Jin, and Z. Nie, "Improving the accuracy of the second-kind fredholm integral equations by using the Buffa-Christiansen functions," *IEEE Transactions on Antennas and Propagation*, vol. 59, no. 4, pp. 1299–1310, Apr. 2011.

[22] S. Yan, J. Jin, and Z. Nie, "Accuracy improvement of the second-kind integral equations for generally shaped objects," *IEEE Transactions on Antennas and Propagation*, vol. 61, no. 2, pp. 788–797, Feb. 2013.

[23] Ö. Ergül and L. Gürel, "Discretization error due to the identity operator in surface integral equations," *Computer Physics Communications*, vol. 180, no. 10, pp. 1746–1752, Oct. 2009.

[24] Ö. Ergül and L. Gürel, *The Multilevel Fast Multipole Algorithm (MLFMA) for Solving Large-Scale Computational Electromagnetics Problems*, Wiley-IEEE, 2014.

[25] L. Gürel and Ö. Ergül, "Contamination of the accuracy of the combined-field integral equation with the discretization error of the magnetic-field integral equation," *IEEE Transactions on Antennas and Propagation*, vol. 57, no. 9, pp. 2650–2657, Sep. 2009.

[26] Y. Beghein, K. Cools, H. Bağcı, and D. D. Zutter, "A space-time mixed galerkin marching-on-in-time scheme for the time-domain combined field integral equation," *IEEE Transactions on Antennas and Propagation*, vol. 61, no. 3, pp. 1228–1238, Mar. 2013.

[27] S. Güler, A. C. Yücel, H. Bağcı, and Ö. Ergül, "Mixed discretization of CFIE in the framework of MLFMA," in Proc. *Progress in Electromagnetics Research Symp. (PIERS)*, 2018, 1500–1505.

[28] S. Güler, H. İbili, and Ö. Ergül, "Mitigating internal resonances of the magnetic-field integral equation via double-layer modeling," in Proc. *European Conf. on Antennas and Propagation (EuCAP)*, 2018.

[29] S. Güler, H. İbili, and Ö. Ergül, "Resonance-free magnetic-field integral equation with double-layer modeling: further improvements," in Proc. *Progress in Electromagnetics Research Symp. (PIERS)*, 2019.

[30] M. B. Woodworth and A. D. Yaghjian, "Multiwavelength three-dimensional scattering with dual-surface integral equations," *J. Opt. Soc. Amer. A*, vol. 11, no. 4, pp. 1399–1413, 1994.

[31] M. Zubair, M. A. Francavilla, D. Zheng, F. Vipiana, and G. Vecchi, "Dual-surface electric field integral equation solution of large complex problems," *IEEE Transactions on Antennas and Propagation*, vol. 64, no. 6, pp. 2577–2582, Jun. 2016.